

MT-03-22

CFD analysis of pot room



Course: MT-03-22

Title: CFD analysis of pot room

This report forms part of the basis for assessing the student's performance in the course.

Group participants: Kristian Aasbø Hansen

Supervisor: Andre Vagner Gaathaug

Project partner: **Hydro Aluminium Karmøy**

Summary:

Hydro Aluminium Karmøy has received media attention due to increased local fluoride emissions. The interest in reducing the emissions from the roof is prioritized. Based on this interest, an optimum location is desirable for a laser-based monitor, which will be located by running a Computation Fluid Dynamic (CFD) simulation.

The object of the presented thesis is to investigate natural convection in a pot room with one pot as the heat source and verify it with experimental data and an ANSYS FLUENT Model. The case setup contains three different geometries, 2D small-scale, 2D, and 3D large-scale.

Numerical simulations are carried out by developing a solver for OpenFOAM, and the finite volume method is employed to solve governing equations. A buoyancy corrected standard k-epsilon, and LRN k-epsilon model is used to simulate turbulence.

The experimental data are collected on a footbridge at the top of the pot room. The full-scale 3D model, validated by experimental data and the ANSYS FLUENT model, shows correct outlet temperature differences but suffers high velocities. Implementing porous zones and further validation will reduce the outlet velocity. The model is not valid for local heat transfer close to heated boundaries, but the wall conditions do not affect the outlet temperature.

The location for the planned laser-based monitor is recommended to be between the footbridge and the monitor wall.

Preface

The master thesis is written at and collaborated with Hydro Aluminum Karmøy, Norway. I would like to thank my supervisors Andre Vagner Gaathaug and Eirik Manger. E. Manger have been helping me with the mesh generation of the large scale, guidance in the cluster and general supervising. Andre's guidance has been helpful through the thesis period. Further, I will like to thank my friend, Sivert. Supplying me with a computer when my computer crashed. Big thanks to my friends for keeping up my social life between my job and thesis period. Lastly, I would like to thank Hydro Aluminium Karmøy for supplying me with an office, work computer, the cluster and cakes.

Karmøy, 14th May 2022

Kristian Aasbø Hansen

Contents

Preface.....	3
Contents	4
Abbreviations	6
Nomenclature	7
1 Introduction	10
1.1 Background	10
1.2 Previous work.....	11
1.3 Outline of thesis.....	11
2 Theory	12
The theory chapter will introduce CFD and aluminum production theory, including different aspects of natural convection.	12
2.1 HF-emission.....	12
2.1.1 <i>Agreements</i>	12
2.1.2 <i>Bayer process</i>	12
2.1.3 <i>Hall-Héroult process</i>	13
2.1.4 <i>Off-gas system</i>	13
2.1.5 <i>Cell coverage</i>	14
2.2 Heat transfer	15
2.2.1 <i>Temperature stratification</i>	15
2.3 Natural convection.....	16
2.3.2 <i>Stack effect</i>	18
2.3.3 <i>Estimation of Ventilation rate</i>	19
2.3.4 <i>Navier Stokes Equation</i>	21
2.3.5 <i>Energy equation</i>	22
2.3.6 <i>Reynolds-average Navier stokes (RANS) equations</i>	22
2.3.7 <i>Validation</i>	25
2.3.8 <i>Discretization</i>	25
2.3.9 <i>Upwind differencing scheme</i>	25
2.3.10 <i>Solution algorithms</i>	26
2.3.11 <i>Porosity</i>	21
2.4 Mesh.....	27
2.4.1 <i>Mesh structures</i>	27
2.4.2 <i>Mesh quality</i>	27
2.5 ANSYS FLUENT.....	28
3 Method	30
3.1 Measurements	30
3.1.1 <i>Temperature and velocity measurements</i>	30
3.2 Solver	32
3.2.1 <i>Small scale</i>	32
3.2.2 <i>Full-scale model</i>	32
4 Preprocessing and Simulation	33
4.1 Assumptions	33
4.2 Mesh.....	33
4.2.1 <i>Small scale</i>	33

4.2.2 <i>Full scale</i>	34
4.3 Boundary conditions	35
4.3.1 <i>2D</i>	35
4.4 System	36
4.4.1 <i>ControlDict</i>	37
4.4.2 <i>DecomposeParDict</i>	37
4.4.3 <i>creatBafflesDict</i>	37
4.5 Constant folder	37
4.6 Sampling and Plotting	37
5 Results	38
5.1 Experimental data	38
5.2 2D cases	39
5.2.1 <i>Small scale</i>	39
5.2.2 <i>Large scale</i>	40
5.2.3 <i>Winter vs summer</i>	41
5.3 3D case	42
5.3.1 <i>Location of the probe mounting</i>	45
5.3.2 <i>Mesh quality</i>	46
5.4 Mesh dependency	46
6 Discussion	48
7 Conclusion	51
7.1 Further work	51
References	52
Appendices	56
Appendix A: Task Description	57
Appendix B	58
Appendix C Experimental data	63
Appendix D: Building Geometry	68
Appendix E 2D OpenFoam	71
Appendix F 2D ANSYS FLUENT	76
Appendix G – 3D OpenFOAM	78
Appendix H- 3D ANSYS FLUENT	83
Appendix I y^+ measurements for 3D model	84

Abbreviations

AP18	Prebake technology, older building
KTP	Karmøy Technology Pilot building, new electrolysis technology
Pot	Electrolysis cell
HF	Hydrogen Fluoride
AF	ANSYS FLUENT
OF	OpenFOAM
LRN	Low Reynolds Number
BAT	Best Available Techniques
PO	Primary oxide
SO	Secondary oxide
HVAC	Heating Ventilation, and Air Condition
RANS	Reynolds-average Navier stokes
SIMPLE	Semi-Implicit Method for Pressure-Link Equations
PISO	Pressure Implicit with Splitting of Operators
AR	Aspect Ratio
GUI	Graphic user interface
EOS	Equation of State
LES	Large Eddy Simulations

Nomenclature

<u>Symbol</u>	<u>Description</u>	<u>unit</u>
q	Heat flux	[W/m ²]
H	Heat transfer coefficient	
T_s	Surface temperature	[K]
T_a	Ambient temperature	[K]
u	Velocity component in x-direction	[m/s]
v	Velocity component in y-direction	[m/s]
w	Velocity component in z-direction	[m/s]
$\frac{\partial u}{\partial x}$	Velocity gradient in x-direction	
$\frac{\partial v}{\partial y}$	Velocity gradient in y-direction	
$\frac{\partial w}{\partial y}$	Velocity gradient in z-direction	
$\frac{dp_\infty}{dx}$	Freestream pressure gradient	
$\frac{\partial^2 u}{\partial y^2}$	Acceleration of velocity component u in y direction	
g	Gravitational forces	[m/s ²]
ρ_∞	Freestream density	[m ³ /kg]
$\Delta\rho$	Density difference	[m ³ /kg]
ρ	Density	[kg/m ³]
β	Volumetric thermal expansion coefficient	[1/T]
$\frac{\partial \rho}{\partial T}$	Density gradient	
T_∞	Surrounding Temperature	[K]
T	Absolute temperature	[K]
Δp	Pressure difference	[Pa]

z	Stack height	[m]
Q	Heat source	[W]
\dot{m}	Mass flow	[kg/s]
ΔT	Temperature difference	[K]
c_p	Specific heat capacity	[J/kgK]
P	Absolute pressure	[Pa]
R	Universal gas constant	[m ³ Pa/molK]
A	Characteristic area	[m ²]
T_{in}	Inlet temperature	[K]
T_{out}	Outlet temperature	[K]
C	Constant	
\dot{V}	Volumetric flow rate	[m ³ /s]
\mathbf{u}	Velocity vector	[m/s]
ϕ	Fluctuating property	
$\frac{\partial(\rho\phi)}{\partial t}$	Change of fluid over time	
$div(\phi\mathbf{u})$	convective term	
$div(\mu grad\phi)$	diffusion term in Naviers Stokes equation	
S_ϕ	Source term	
Φ	Mean flux flow	
ϕ'	turbulent fluctuations	
u'	Mean velocity component in x-direction	[m/s]
v'	Mean velocity component in y-direction	[m/s]
w'	Mean velocity component in z-direction	[m/s]
τ_{ij}	Shear stress vector	[Pa/ m ²]
y^+	Dimensionless length scale	
V	Velocity scale	[m/s]
l	Length scale	[m]

k	turbulent kinetic energy	[J/kg]
ϵ	turbulence dissipation rate	[m ² /s ³]
μ_t	Eddy viscosity	[Pa s]
C_μ	Dimensional constant	
P	Production of ϵ and k	
B	buoyant turbulence production of ϵ and k	
S	Strain stress	[Pa]
$C_{i\epsilon}$	turbulent constant	
$C_{2\epsilon}$	turbulent constant	
$C_{3\epsilon}$	turbulent constant	
σ_k	turbulent Prandtl number	
σ_ϵ	turbulent Prandtl number	
σ_t	turbulent Prandtl number	
R_f	flux Richardson	
f_μ, f_1, f_2	Turbulence model functions (damping functions)	
τ_w	Wall shear stress	[Pa]
u_τ	friction velocity	[m/s]
U	Mean flow velocity	[m/s]
K	specific permeability constant	[m ²]
μ	dynamic viscosity	[Pa s]
φ	permeability	
ρ_0	Operating density	[kg/m ³]
$p'_s = p_{rgh}$	Dynamic pressure without hydrostatic pressure	[Pa]

1 Introduction

This thesis was written in collaboration with Hydro Aluminum Karmøy and the University of South-Eastern Norway (USN). The upcoming sub-chapters will describe the background and the objective of the thesis.

1.1 Background

There has been media attention to the increase in local fluoride emissions, and Hydro Aluminum Karmøy is prioritizing the reduction of emissions over the roof from the pot room, both at AP18 and KTP (Karmøy Technology Pilot). The Figure 1-1 display emissions increased in 2018 due to the start-up of KTP. The interplay between mechanical encapsulation of cells through good covers, collars, drain doors, and the use of forced extraction, along with extraction volume and proper balancing of the pots, forms the interface with the gas purifier. The gas purifier traps the exhaust gas from the electrolysis cells and therefore it is essential to keep the leakage area to a minimum.

Hydro Aluminium Karmøy

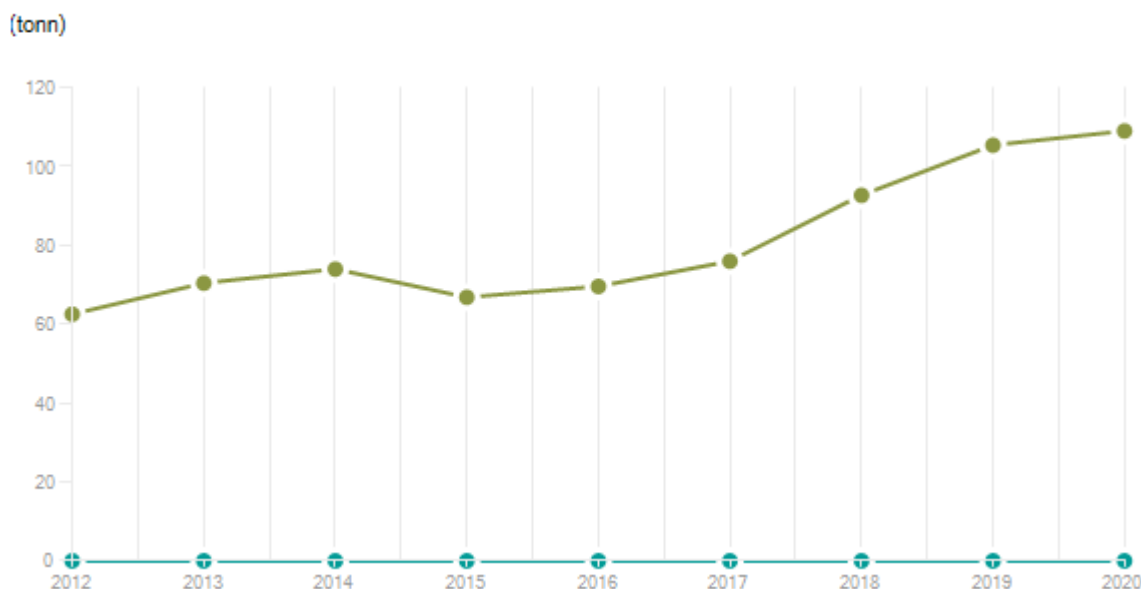


Figure 1-1 – Releases of Fluorides (in ton) per year. [1]

AP18 is divided into ten different sections, where two sections are changing anodes every 8 hours. There are 28-33 electrolysis cells in each section, containing 16 anodes each. When these anodes are changed, a maximum of two pots are allowed to remove covers to access the anodes due to the capacity of the gas purification system.

Today, there are located two point monitors in each section for the Hydrogen Fluoride (HF) emissions. Still, Hydro Aluminum Karmøy is planning to install a laser-based monitor, to replace the two point monitors. Hydro is interested in determining the pot room flow structure to locate the optimal location for the planned laser-based monitor. The laser-based monitor will increase the accuracy, since the emissions change location over the roof due to anode change.

With the laser-based monitor, there will be better monitoring of each shift to improve the routines of cover handling, resulting in lower emissions.

To determine the flow structure in the pot room, a CFD model will provide the information. The model will be developed for natural convection in a pot room and validated against experimental data and an ANSYS FLUENT (AF) model.

1.2 Previous work

W. F. de Gids made a prediction model for calculating the airflow through buildings and used the prediction model with validation of measurements of an 87 000m³ industrial building to determine the relationship between airflow pattern, temperature distribution, and spread of dust. [2]

A group of researchers investigated the effect of boundary conditions on natural convection and fluid flow on a vertical channel, with one heated wall, for a working fluid with $Pr = 0.71$ and $Ra = 5 \times 10^5$. Bernoulli's theorem was used for the study, which assumes stationary, incompressible, and inviscid fluid flow with a uniform pressure at the inlet. They studied the boundary conditions and the flow pattern in a vertical channel for different heights relative to the inlet area. They proved that the buoyancy effect is more dominating when the height increases, close to the wall, with backflow at the colder side. [3]

S-H. Peng, L. Davidson investigated the prediction of the buoyancy effect by checking the performance of low Reynolds number (LRN) $k-\omega$ with comparisons of LRN $k-\epsilon$ and experimental data. Both models showed sensitivity to refined mesh in predicting the transitional boundary layer flow along a vertical wall for Rayleigh number of 5×10^{10} . They also proved delayed transitional flow from the inlet and not grid-dependent in the freestream. [4]

Based on these discoveries, none of them have combine natural convection on a large industrial building with a heat source.

1.3 Outline of thesis

- Chapter 2 describes the production of aluminum, CFD (Computational Fluid Dynamics) and natural convection.
- Chapter 3 describes the method done for this thesis.
- Chapter 4 describes the setup of the simulations.
- Chapters 5, 6 and 7 present the results, discussion, and conclusion, respectively.

2 Theory

The theory chapter will introduce CFD and aluminum production theory, including different aspects of natural convection.

2.1 HF-emission

HF gas is a chemical compound generated in the production of Aluminium, which will be described in Chapter 2.1.3. The following topics will focus on international and national agreements, the Bayer process, Hall-Héroult, anode change, and the gas-of system.

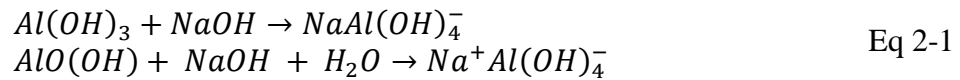
2.1.1 Agreements

In 2016, the European parliament established Best Available Techniques (BAT) conclusions, with recommended total HF emissions with the available cleaning process, for new and established plants. Hydro Aluminium Karmøy undergoes the BAT 67 technology, with complete coverage of the cell and an off-gas treatment, considering HF generation from the bath (electrolyte) and carbon anode consumption. The existing technology regulates the limits of ≤ 0.6 kg/ton Al for prebake. [5]

Hydro Karmøy and the Norwegian Environment Agency have agreed on a deal for AP18 (section K3, K4, and K5) with the limit of 0.4 kg/ton Al and a monthly average emission to 11 kg/h and 8 kg/h for an annual average. These limits are for the sum of HF gas and particulate-bound fluorides. [6]

2.1.2 Bayer process

The raw material for aluminum is Bauxite, which contains a high amount of aluminum hydroxide ($Al(OH)_3$). The Bauxite is refined in the Bayer process, where the Bauxite is crushed and digested in a recycled sodium hydroxide (NaOH) and lime solution at high temperatures. [7]



In the reaction in the NaOH solution in Eq 2-1, most of the minerals in the ore are dissolved, resulting in an unsolvable red mud. Removal of the red mud is done by filtration/sedimentation. After the filtration, the process is reversed using precipitation, where the solution is cooled and fed by $Al(OH)_3$, shown in Eq 2-2.



In Eq 2-2, NaOH is separated and recycled, and then by calcinating, converted to Aluminum oxide, containing water from the reaction shown in Eq 2-3.



2.1.3 Hall-Héroult process

The aluminum is produced using an electrolysis cell containing an anode, cathode, and electrolyte. The anode is made from coke, prebaked with high carbon content, and carried by an anode stud. The cathode is melted aluminum, and the electrolyte is molten cryolite that contains aluminum fluoride (AlF) and calcium chloride to lower the temperature and increase the conductivity. [8] [9]

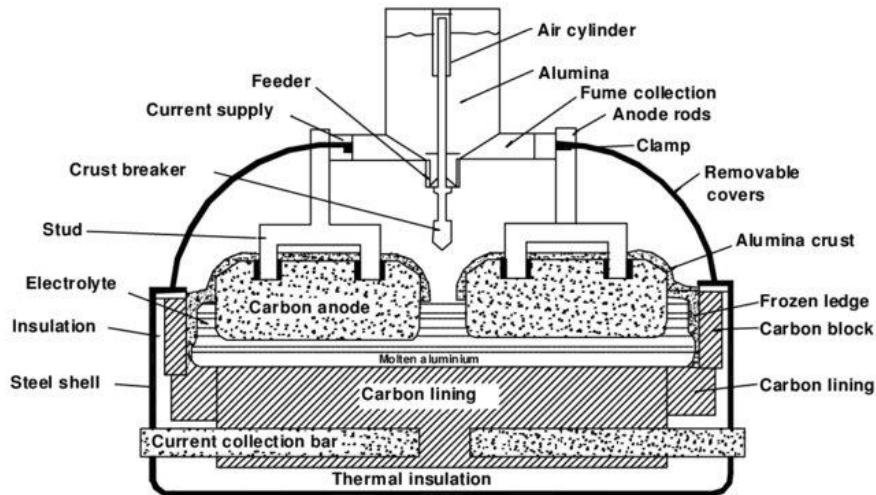


Figure 2-1 Overview of an electrolysis cell [9]

The recycled AlF are added to the electrolyte with the help of the crust breaker, as shown in Figure 2-1. The recycling process is described in Chapter 2.1.4. The aluminum oxide reacts in the electrolyte, according to Eq 2-4, and forms aluminum and CO₂, with byproducts as HF, CO, CF₄, C₂F₆, etc.



As described in Chapter 2.1.2, the aluminum oxide contains water, which is hydrated when exposed to a hot environment, also called loss of ignition. The water reacts with the cryolite, having F-ions to form HF-gas.

2.1.4 Off-gas system

The off-gas system uses a physical cleaning method using large-scale bag-filters and absorption to remove the HF gas. The generated gas in the pot is sucked through the duct, and into a reactor, before the bag-filters. In the reactor, the primary oxide (PO) and recycled secondary oxide (SO) is added and transported to the bag-filters as shown in Figure 2-2. PO is another name for Aluminium oxide. The entering gas, with SO and PO passes the bag-filters, where PO and SO mounts to the bag-filters. PO and SO contains large surface and are used as adsorption material for the HF gas. The passing HF gas and adsorbs the passing HF gas. During the reaction time, the oxide bonds with the HF gas to generate enriched oxide, called secondary oxide, resulting in an approximate 1.7 weight increase due to fluoride.

The bag filter has a cleaning cycle using pulsing air, where the secondary oxide is partly recycled into the reactor chamber and partly transported to buffer tanks, as shown in Figure

2-2. As described in the chapter above, the secondary oxide from the buffer tanks is fed to the pot.

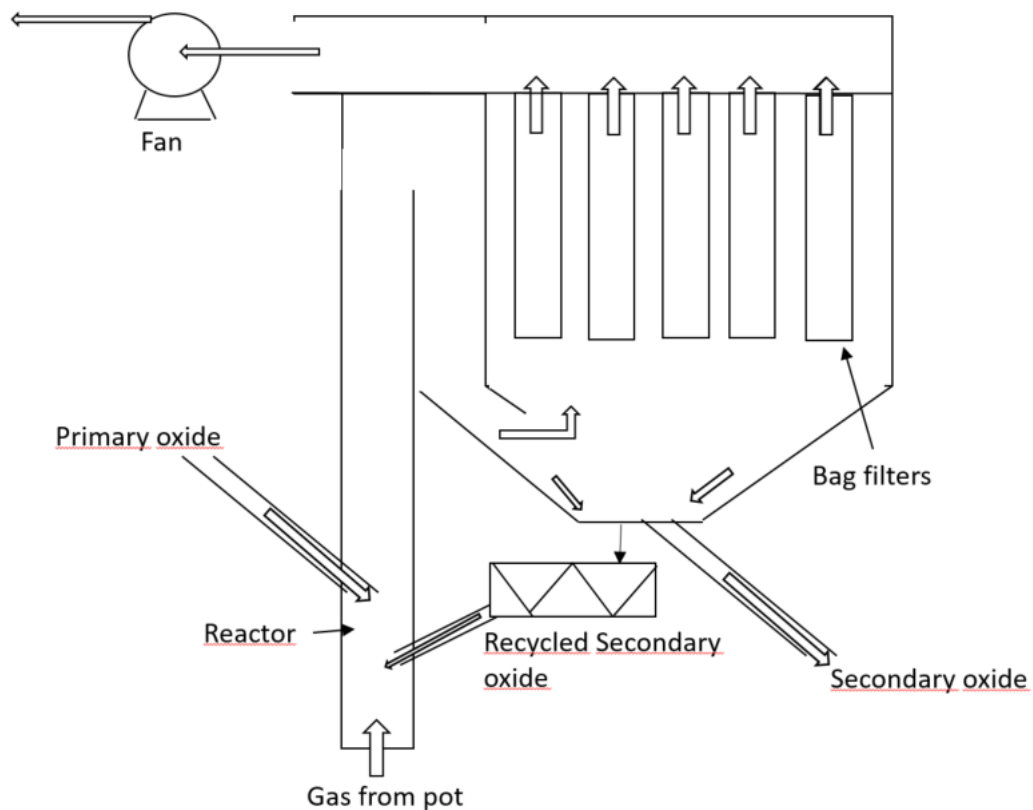


Figure 2-2: The recycling process of aluminum oxide

Sometimes a bag-filter breaks and let HF gas through. HF gas is transported to the bottom of the absorption towers and reacts with a cloud of seawater. The seawater enters at the absorption tower top and is sprayed through nozzles generating the seawater cloud. Seawater naturally contains limestone, which neutralizes and absorbs the HF gas.

2.1.5 Cell coverage

The pots are fully covered in normal circumstances, but every 40th hour, anodes in the cell must be replaced. For reduction of emission, the procedure of the anode change is described as follows: A maximum of two electrolysis cells can be worked on simultaneously, which means that two covers on each cell can be open when the off-gas system is turned on. If these two limits exceed, the off-gas system is choked due to capacity, and all the emitted gas goes through the roof. In a practical manner, these procedures are not always followed, and that is why better monitoring of the emission through the roof is prioritized. The measurements are directly coupled to a team performance system, where each shift gets a score for the total amount of emitted gas through the roof.

2.2 Heat transfer

Heat transfer occurs in three forms, conduction, convection, and radiation. The focus of the thesis is convection in the form of natural convection heat transfer.

Heat transfers from a hot surface to the surrounding by convection, which combines advection and conduction. Advection and conduction is the transport of particles by bulk motion and surface heat transfer, respectively. A closer study on the heat transfer into the surroundings and governing equations are discussed in the following chapter.

Heat transfer for the general energy from a heat source is given in Eq 2-5, describing the heat flux (q) from a heat source, with a given heat transfer coefficient (h) from the surface temperature (T_s) to the environmental temperature (T_a).

$$q = h(T_s - T_a) \quad \text{Eq 2-5}$$

2.2.1 Temperature stratification

Extra fans can be installed in (Heating Ventilation, and Air Condition) HVAC systems to reduce temperature stratification along with the boundary layer. As shown in Figure 2-3, a backflow appears because mass flow differences are higher at the outlet than at the inlet to compensate. *The recirculating fluid increases the fluid temperature in the outer part of the boundary layer. This leads to temperature stratification alongside the boundary layer causing the boundary layer growth to be affected owing to the decreased buoyancy force¹.* [10] To provoke the effect, increasing the inlet flow will reduce recirculation and temperature stratification. [11]

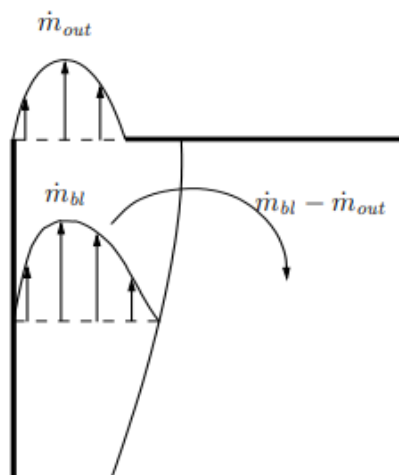


Figure 2-3: Temperature stratification due to recirculation [11]

¹ [14]

2.3 Natural convection

Convective heat transfer is divided into three types of phenomena, natural convection, forced convection, and mixed convection.

The focus of the thesis is natural convection due to density gradients. This means that when the temperature increases, the density decreases, and the fluid is naturally moving upwards against gravitational forces, which are known as the buoyancy forces. In a closed domain, and the heated plate is at the bottom, the fluid will be stable. However, if there is a closed case and the heated plate is at the top, the density gradient will be larger than 0, resulting in an unstable fluid, shown in Figure 2-4.

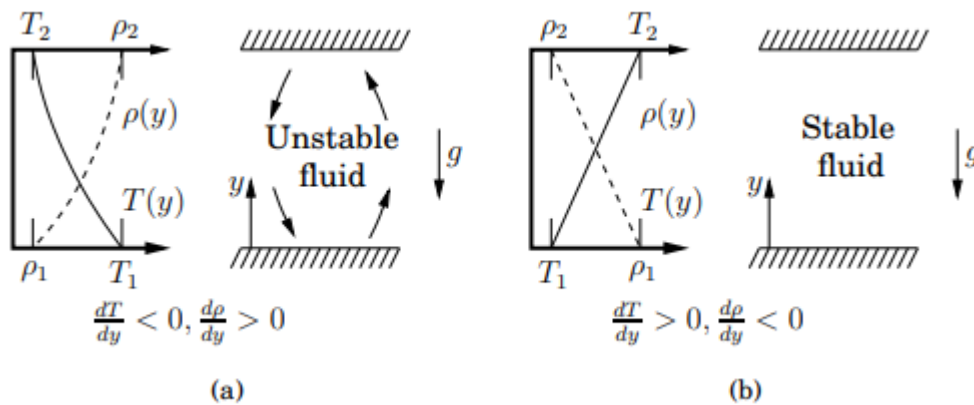


Figure 2-4 – Case a, heated upper plate. Case b, heated lower plate [12]

2.3.1.1 Free convective flow

For a free convection flow, fluid from a heated object is submerged in a quiescent fluid. The hot fluid rises due to buoyancy forces, and entrains more fluid from the quiescent region. A plume is formed, and the width increases with increased distance from the heated object but eventually dissipates due to viscous forces and reduction in the buoyancy due to cooling, as shown in Figure 2-5. [12]

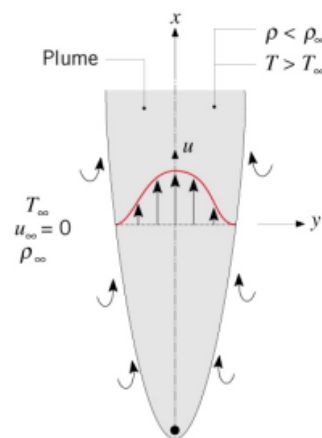


Figure 2-5 Plume generation from a heat source [12]

2.3.1.2 Vertical plate

Free convection on a heated vertical plate, with a no-slip condition, creates a velocity profile close to the wall, bounded by the wall and the surrounding fluid. The temperature profile ($T_s > T_\infty$) perpendicular to the wall decreases when the distance from the heated vertical plate increases, resulting in lower density and higher velocities close to the wall, as shown in Figure 2-6.

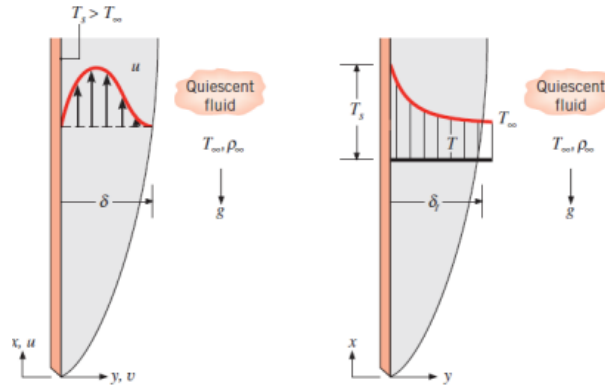


Figure 2-6 x-component velocity boundary layer and temperature boundary layer [12]

2.3.1.3 Governing Equations

Considering a laminar boundary layer for a vertical plate, the flow is assumed to be two-dimensional, steady-state with constant property conditions and valid boundary layer approximations. If the gravity is acting in a negative x-direction, the x-momentum equation can be considered, shown in Eq 2-6.

$$u \frac{\partial u}{\partial x} + v \frac{\partial v}{\partial y} = -\frac{1}{\rho} \frac{dp_\infty}{dx} - g + v \frac{\partial^2 u}{\partial y^2} \quad \text{Eq 2-6}$$

The free stream pressure gradient ($\frac{dp_\infty}{dx}$) in the quiescent region outside the boundary layer, where outside the boundary layer, the equation reduces to Eq 2-7.

$$\frac{dp_\infty}{dx} = -\rho_\infty g \quad \text{Eq 2-7}$$

Substitute Eq 2-7 into the x-momentum equation, the following expression is shown in Eq 2-8.

$$u \frac{\partial u}{\partial x} + v \frac{\partial v}{\partial y} = g \left(\frac{\Delta \rho}{\rho} \right) + v \frac{\partial^2 u}{\partial y^2} \quad \text{Eq 2-8}$$

The $\Delta \rho$ describes difference between the freestream and local density. This term represents the buoyancy force, and if the density changes are only due to temperature changes, then this term can be related to the volumetric thermal expansion coefficients, shown in Eq 2-9.

$$\beta = \frac{1}{\rho} \frac{\partial \rho}{\partial T} \quad \text{Eq 2-9}$$

The volumetric thermal expansion coefficient is a measure of the density change due to temperature changes in a constant pressure. By using this approximation, the Boussinesq approximation is formed, shown in Eq 2-10. The Boussinesq approximation ignores density change due to pressure and only considers a linear dependency on temperature. [13] [14]

$$\beta \approx \frac{1}{\rho} \frac{\rho_{\infty} - \rho}{T - T_{\infty}} \quad \text{Eq 2-10}$$

2.3.1.4 Horizontal and inclined plates

For buoyancy-driven flow, with a heated horizontal plate, the fluid is forced to flow horizontally before it can ascend at the edge, resulting in an ineffective convective heat transfer. [12]

For a buoyancy driven heated plate warmer than the environmental temperature, the temperature profile is displayed in Figure 2-7. The flow moves along the plate before the fluid starts ascending, due to the buoyancy forces.

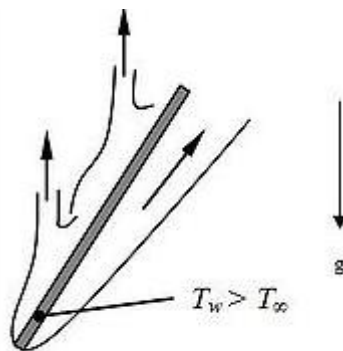


Figure 2-7: Natural convection on a heated inclined heated plate inspired by [12]

2.3.2 Stack effect

The buoyancy forces that are created due to density gradients can also be referred to as the stack effect. When the temperature is higher inside the building, negative pressure differences occur at the bottom part of the building, creating vacuum. The vacuum allow the air to enter at the bottom part of the building creating positive pressure differences at the top of the building. Displayed by Figure 2-6, a neutral pressure plane describes the pressure differences at the inlet and outlet. The neutral pressure plane varies with size of the openings, temperature inside the building and wind, due to Bernoulli's theorem. [15]

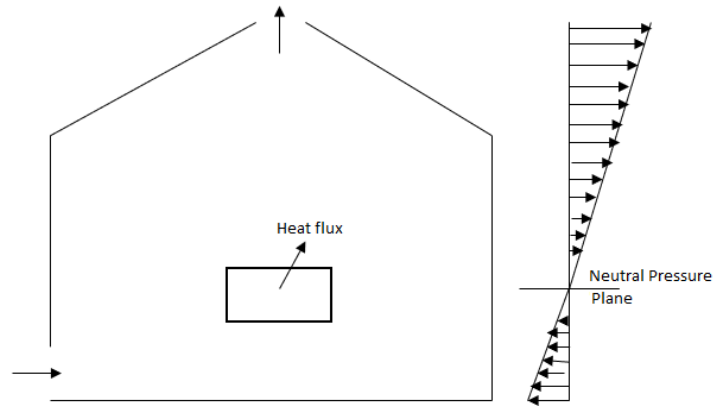


Figure 2-8 Stack effect of a building with a heat source

2.3.3 Estimation of Ventilation rate

An estimation of the ventilation rate over the roof can be determined, which will be used as part of the validation of the model. Natural ventilation is, in general, governed by three equations, stack effect (Eq 2-11), dynamic pressure loss drop due to flow (Eq 2-12), and temperature increase (Eq 2-13). [15]

$$\Delta p = zg\Delta\rho \quad \text{Eq 2-11}$$

$$\Delta p = \frac{\rho v^2}{2} \quad \text{Eq 2-12}$$

$$Q = \dot{m}c_p\Delta T \quad \text{Eq 2-13}$$

Where z is the stack high, g is the gravitational force, ΔT temperature difference, ρ is the density, v is the velocity, \dot{m} is the mass flow, c_p specific heat capacity, and Q heat source pressure difference. In addition, the ideal gas law is introduced, where R is the universal gas constant, P absolute pressure, T temperature, molar flow and volumetric flow.

$$P = \rho RT \quad \text{Eq 2-14}$$

2.3.3.1 Mass flow rate

Combining Eq 2-14 with the relationship of volumetric flow rate, velocity, density, mass flow rate, and characteristic area gives Eq 2-15.

$$\Delta p = \frac{\dot{m}^2}{2A^2\rho} \quad \text{Eq 2-15}$$

Further combining ideal gas law.

$$\Delta p = \frac{\dot{m}^2 RT}{2A^2 P} \quad \text{Eq 2-16}$$

For Eq 2-16, the density difference is solved with ideal gas law resulting in absolute pressure and temperature difference. The absolute pressure and temperature difference for the pot room are neglectable, and the pressure and temperature difference for the inlet and outlet are assumed equal to zero, shown in Eq 2-17.

$$\Delta p = zg\Delta\rho = \frac{zg\Delta P}{R} \left(\frac{1}{T_{out}} - \frac{1}{T_{in}} \right) = \frac{zg\Delta P}{R} \left(\frac{\Delta T}{T_{in}T_{out}} \right) \approx \frac{zgP\Delta T}{RT^2} \quad \text{Eq 2-17}$$

Combining Eq 2-13, Eq 2-16 and Eq 2-17.

$$\frac{\dot{m}^2 RT}{2A^2 P} = \frac{zgPQ}{R\dot{m}c_p T^2} \quad \text{Eq 2-18}$$

Rearranging Eq 2-18 and setting the constants (g, c_p, z, and R) to one constant, C.

$$\dot{m} = C \frac{\sqrt[3]{P^2 Q A^2 z}}{T} \quad \text{Eq 2-19}$$

Eq 2-19 is an estimation of ventilation for mass flow rate, which shows the mass flow rate is inversely proportional to temperature.

2.3.3.2 Volumetric flow rate

Further, the estimation for volumetric flow is continued using Eq 2-19, replacing \dot{m} with $\dot{V}\rho$ and combining the ideal gas law, resulting in Eq 2-20.

$$\dot{V} = C \sqrt[3]{\frac{zQA^2}{P}} \quad \text{Eq 2-20}$$

The volumetric flow rate is proven to be independent of the temperature for ventilation in the pot room, meaning the volumetric flow rate will remain constant through summer and winter. However, the wind will affect the volumetric flow rate and mass flow.

2.3.4 Porosity

The porosity of a medium is defined by small holes occupied by fluid inside a solid element. Walls contain small deformations, allowing the fluid to flow through the pores. For a single-phase, the pores are saturated by the fluid.

There are magnetic fields in the pot room, and the generation of drag is neglectable. [26]

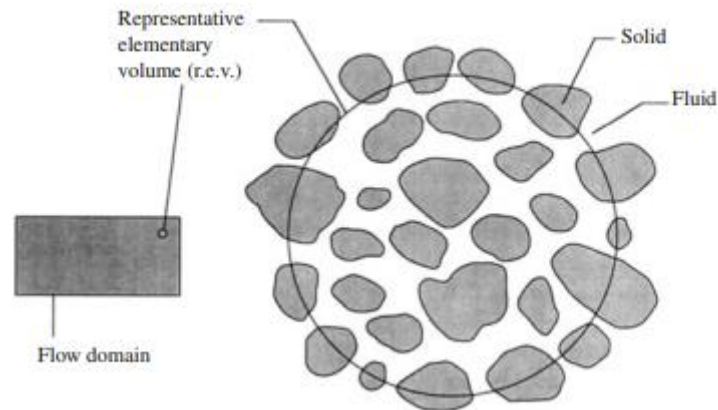


Figure 2-9: Illustration of intermediate size relative the flow domain in the pores. [26]

Darcy's law can be applied for flow-through porous zones, describing the proportionality of flow and pressure differences. The following Eq 2-41 can describe the relationship.

$$u = -\frac{K}{\mu} \frac{\partial P}{\partial x} \quad \text{Eq 2-21}$$

Where $\frac{\partial P}{\partial x}$ represents the pressure gradient, K is the specific permeability constant with the length scale powered by two and μ is the dynamic viscosity. The coefficient K describes the medium's geometry allowing fluid to flow through the pores. For a single-phase flow, the K is simplified to permeability, ϕ . For concrete, the permeability is equal to 0.1. [26]

2.3.5 Navier Stokes Equation

Navier Stokes Equation is the universal law of physics and can be used to model any type of fluid, gas, and solids to describe their behavior, movements, and characteristics.

Conservation of mass describes the fluid that moves around, where no mass is added or removed, mass is conserved, shown in Eq 2-22.

$$\text{div } \mathbf{u} = 0 \quad \text{Eq 2-22}$$

Conservation of momentum is based on Newton's second law for a incompressible Newtonian fluid and is described in Eq 2-23. The first term is the rate of change of the fluid element, the second term is the convective term, the third term is the pressure gradient, the fourth is the diffusion term, and the last is the source term.

$$\rho \left(\frac{\partial(\phi)}{\partial t} + \text{div}(\phi \mathbf{u}) \right) = -\frac{1}{\rho} \frac{\partial P}{\partial x} + \text{div}(\mu \text{grad} \phi) + S_\phi \quad \text{Eq 2-23}$$

2.3.6 Energy equation

The energy equation is governed by the first law of thermodynamics, describing the rate of energy of the bulk flow as equal to the rate of heat added to the bulk flow plus the rate of work done on the bulk flow. For an ideal compressible gas, the energy equation can be shown in Eq 2-24.

$$\frac{\partial(\rho i)}{\partial t} + \text{div}(\rho i \mathbf{u}) = -p \text{div} \mathbf{u} + \text{div}(k \text{grad} T) + S_i \quad \text{Eq 2-24}$$

Where p and i are ρRT and $C_v T$, respectively.

2.3.7 Reynolds-average Navier stokes (RANS) equations

A direct modeling of Navier Stokes equations in turbulence flow are extremely time consuming and complicated, and impossible in most of 3D cases. For reduction of time and cost, time average equations are included for motion of the fluid, which are described by Reynolds decomposition to investigate the mean (Φ) flow and turbulent fluctuations (ϕ') in the Navier Stokes equations, shown in Eq 2-25.

$$\phi = \Phi + \phi' \quad \text{Eq 2-25}$$

Resulting in turbulent stresses that represent the effect of turbulent mixing and momentum transfer between fluid layers.

$$\frac{\partial(\Phi)}{\partial t} + \text{div}(\rho \Phi \mathbf{U}) = \frac{1}{\rho} \text{div}(\Gamma_\Phi \text{grad} \Phi) + \left[-\frac{\partial(\overline{u'\phi'})}{\partial x} - \frac{\partial(\overline{v'\phi'})}{\partial y} - \frac{\partial(\overline{w'\phi'})}{\partial z} \right] + S_\phi \quad \text{Eq 2-26}$$

The extra term in Eq 2-26 represents Reynold stresses and results in six additional stresses into the momentum equation, three normal and three shear stresses.

$$\tau_{ij} = \rho \begin{pmatrix} \overline{u'u'} & \overline{u'v'} & \overline{u'w'} \\ \overline{u'v'} & \overline{v'v'} & \overline{v'w'} \\ \overline{u'w'} & \overline{v'w'} & \overline{w'w'} \end{pmatrix} \quad \text{Eq 2-27}$$

Solving Eq 2-27, a RANS solver is implemented for the calculation of the fluctuating velocities. k- ϵ model is an universal RANS model, proven to be stable and robust for the industry. [13] One disadvantage is the boundary layer for k-epsilon, where it is valid for $30 < y^+ < 500$.

2.3.7.1 Buoyancy corrected standard k- ϵ model

Knowing turbulence flow is convecting and diffuses through the flow and isn't fixed at some distance from the wall, the k - ϵ is introduced. Solving the transport equation, for turbulence

quantities, the turbulent kinetic energy, k , and turbulence dissipation rate, ϵ , the eddy viscosity can be solved by defining a velocity scale V and length scale l . [13]

$$V = k^{\frac{1}{2}} \quad \text{Eq 2-28}$$

$$l = \frac{k^{\frac{3}{2}}}{\epsilon} \quad \text{Eq 2-29}$$

Combining Eq 2-28 and Eq 2-29, the eddy viscosity can be solved given in Eq 2-30.

$$\mu_t = C\rho\nu l = \frac{\rho C_\mu k^2}{\epsilon} \quad \text{Eq 2-30}$$

Jones and Launder proposed k - ϵ model, using two extra PDEs in the transport equation to determine Reynold stresses. [13] [16] Further, Rajesh K. and Anupam D. provided an evolution of the equations for buoyancy corrected turbulence models. [17]

$$\begin{aligned} \frac{\partial(\bar{\rho}k)}{\partial t} + \frac{\partial(\bar{\rho}k\tilde{u}_j)}{\partial x_i} &= \frac{\partial}{\partial x_i} \left(\left(\mu + \frac{\mu_t}{\sigma_k} \right) \frac{\partial k}{\partial x_i} \right) + P + B - \rho\epsilon \\ \frac{\partial(\bar{\rho}k)}{\partial t} + \frac{\partial(\bar{\rho}k\tilde{v}_j)}{\partial y_i} &= \frac{\partial}{\partial y_i} \left(\left(\mu + \frac{\mu_t}{\sigma_k} \right) \frac{\partial k}{\partial x_i} \right) + P + B - \rho\epsilon \\ \frac{\partial(\bar{\rho}k)}{\partial t} + \frac{\partial(\bar{\rho}k\tilde{w}_j)}{\partial z_i} &= \frac{\partial}{\partial z_i} \left(\left(\mu + \frac{\mu_t}{\sigma_k} \right) \frac{\partial k}{\partial z_i} \right) + P + B - \rho\epsilon \end{aligned} \quad \text{Eq 2-31}$$

$$\begin{aligned} \frac{\partial(\bar{\rho}\epsilon)}{\partial t} + \frac{\partial(\bar{\rho}\epsilon\tilde{u}_j)}{\partial x_i} &= \frac{\partial}{\partial x_i} \left(\left(\mu + \frac{\mu_t}{\sigma_k} \right) \frac{\partial \epsilon}{\partial x_i} \right) + C_{i\epsilon} \frac{\epsilon}{k} P + C_{1\epsilon}(1 - C_{3\epsilon}) \frac{\epsilon}{k} B - C_{2\epsilon} \bar{\rho} \frac{\epsilon^2}{k} \\ \frac{\partial(\bar{\rho}\epsilon)}{\partial t} + \frac{\partial(\bar{\rho}\epsilon\tilde{v}_j)}{\partial y_i} &= \frac{\partial}{\partial y_i} \left(\left(\mu + \frac{\mu_t}{\sigma_k} \right) \frac{\partial \epsilon}{\partial y_i} \right) + C_{i\epsilon} \frac{\epsilon}{k} P + C_{1\epsilon}(1 - C_{3\epsilon}) \frac{\epsilon}{k} B - C_{2\epsilon} \bar{\rho} \frac{\epsilon^2}{k} \\ \frac{\partial(\bar{\rho}\epsilon)}{\partial t} + \frac{\partial(\bar{\rho}\epsilon\tilde{w}_j)}{\partial z_i} &= \frac{\partial}{\partial z_i} \left(\left(\mu + \frac{\mu_t}{\sigma_k} \right) \frac{\partial \epsilon}{\partial z_i} \right) + C_{i\epsilon} \frac{\epsilon}{k} P + C_{1\epsilon}(1 - C_{3\epsilon}) \frac{\epsilon}{k} B - C_{2\epsilon} \bar{\rho} \frac{\epsilon^2}{k} \end{aligned} \quad \text{Eq 2-32}$$

Eq 2-31 and Eq 2-32 describes the rate of change, transport by convection and diffusion, rate of production (P and B) and destruction of k and ϵ , respectively. P denotes the production due to mean shear stresses.

$$P = \mu_t S^2 \quad \text{Eq 2-33}$$

In Eq 2-33, S denotes the strain stress, shown in Eq 2-33.

$$S = \sqrt{2\bar{S}_{ij}\bar{S}_{ij}} \quad \text{Eq 2-34}$$

The buoyant turbulence production term, B, is denoted in Eq 2-35.

$$\begin{aligned} B &= g_j \overline{\rho' u_j} = -\frac{3C_\mu k}{3\sigma_t \epsilon} \left(\overline{u_j u_k} \frac{\partial \bar{\rho}}{\partial x_k} \right) g_j \\ B &= g_j \overline{\rho' v_j} = -\frac{3C_\mu k}{3\sigma_t \epsilon} \left(\overline{v_j v_k} \frac{\partial \bar{\rho}}{\partial y_k} \right) g_j \\ B &= g_j \overline{\rho' w_j} = -\frac{3C_\mu k}{3\sigma_t \epsilon} \left(\overline{w_j w_k} \frac{\partial \bar{\rho}}{\partial z_k} \right) g_j \end{aligned} \quad \text{Eq 2-35}$$

Launder and Spalding suggested experimental data for the turbulent Prandtl number (σ_t) for kinetic energy and dissipation, including C_μ , $C_{i\epsilon}$, $C_{2\epsilon}$ [18]. Rajesh K. and Anupam D compared previous studies for the turbulent constant $C_{3\epsilon}$, varying between 0.3-1.0 without affecting the computations.

Table 2-1: Model Coefficients [18]

C_μ	$C_{i\epsilon}$	$C_{2\epsilon}$	$C_{3\epsilon}$	σ_k	σ_ϵ	σ_t
0.09	1.44	1.92	0.3-1.0	1.00	1.30	0.85

For modeling the turbulent Prandtl number (σ_t), Benodekar proposed a function of flux Richardson using the expression in Eq 2-36. [19]

$$\sigma_t = \frac{0.7(1 - R_f)^2}{1 - \frac{R_f}{0.15}} \quad \text{Eq 2-36}$$

Where the flux Richardson is defined in Eq 2-37.

$$R_f = -\frac{B}{P + B} \quad \text{Eq 2-37}$$

For the turbulence model for a plume, σ_t is equal to 0.85, as given in Table 2-1. [20]

The k- ϵ model is not valid for swirling flow interrupting the turbulence and rapid strain stress change. For improving the strain stress modeling, RNG k- ϵ model is recommended. [13]. Rajesh and Anupam (2014) proved the standard k- ϵ model to be valid for turbulence thermal plume, validating with experimental data. [17]

2.3.7.2 LRN k- ϵ model

Low Reynolds Number flow regions, where the viscous damping effects are essential for turbulence, are not applicable for the standard k- ϵ model. The damping functions (f_μ , f_1 , f_2) are able to solve the turbulent transport equation for the viscous sublayer, and separated and reattached flow in freestream. [21] For adjusting the LRN k- ϵ model for heat transfer, Nagano (1990) introduced improved damping functions and turbulent constants σ_k , $C_{i\epsilon}$ and $C_{2\epsilon}$ constants. [22]

2.3.7.3 Wall boundary layer

The boundary layers close to the wall divide into three different regions: laminar, transitional, and turbulence regions. For the k-epsilon model, it is only valid for the turbulence region. For the inner region, viscous forces dominate, and the shear stress close to the wall is approximately equal to the wall shear stress. Close to the surface of the boundary layer, three wall functions are introduced: Viscous sublayer ($0 < y^+ < 5$), buffer layer ($5 < y^+ < 30$), and inertial sublayer ($30 < y^+ < 500$). The inertial sublayer is the turbulent region close to the wall, called the log-law layer. In the standard k- ϵ model, the non-dimensional distance (y^+) from the wall is equal to the inertial sublayer. Eq 2-38 describes the wall condition based on the shear stress (τ_w) close to the wall, the friction velocity (u_τ), which is a function of viscous forces, distance from the wall, and the fluid density.

$$y^+ = \frac{U}{\sqrt{\frac{\tau_w}{\rho}}} = \frac{U}{u_\tau} \quad \text{Eq 2-38}$$

2.3.8 Validation

The complexity of the pot room, with different length scales, vertical and horizontal surfaces, two inlets, and one outlet, creates difficulties in validating the model theoretically. For previous experimental data, C. Suvanjumrat validated a convective airflow for a k-ε model, setting up multiple temperatures and velocity measurements. With validation, the CFD model deviated 3% from experimental data. [23] Jones and Launer experimented with forced convection when suggesting a LRN k-ε model for a natural flow. [24]

Experimental data have to be included when validating the model. Experimental data for the case were measured at the top of the pot room, described in section 3.1.1.

2.3.9 Discretization

The discretization process using the finite volume method computes the solution at the centroid of every cell in the mesh solution at the centroid of every cell in the mesh. As shown in Figure 2-10, Cell P is where all the computed flow variables are stored, the same for neighbor cells W and E. The unknown variables are the calculated cell faces located on faces w and e. These unknown variables can be scalars and vectors and can be solved using different methods for solving. They can be referred to as face interpolation schemes since they are interpolated at the face field (ϕ_i) at the given cell face at to surrounding cells.

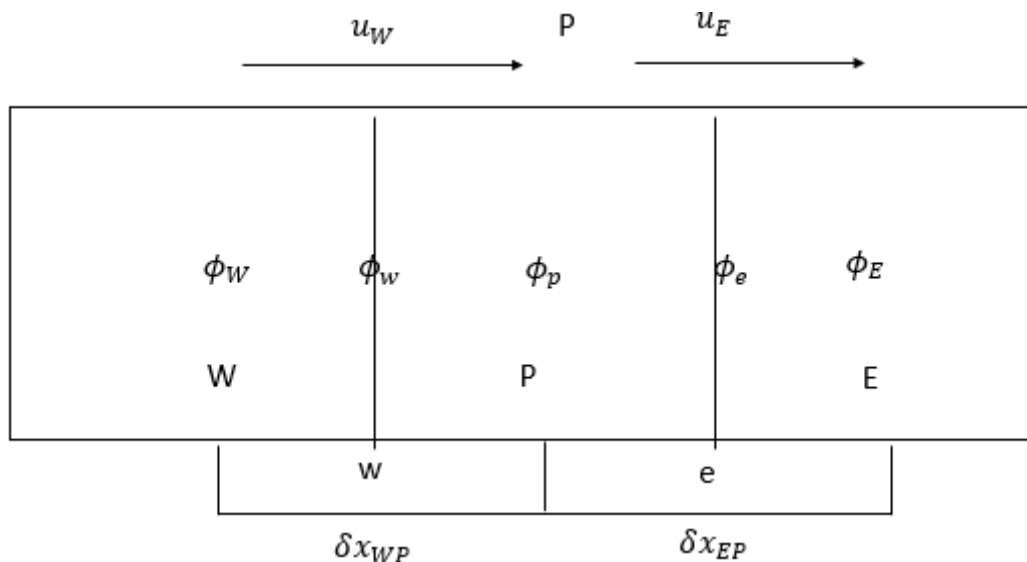


Figure 2-10: Control volume for one dimensional flow at node P, inspired by [13]

2.3.10 Upwind differencing scheme

This scheme is based on upwind differencing that is used for the convective term and depends on the mass flux through the cell face, which can describe the flow direction when determining

the value of the cell face, shown in Eq 2-39. The cell face is denoted by the product of the density, area, and velocity.

$$\phi_i = \begin{cases} u_w > 0, u_e > 0 \rightarrow \phi_w = \phi_W \text{ and } \phi_e = \phi_P \\ u_w < 0, u_e < 0 \rightarrow \phi_w = \phi_P \text{ and } \phi_e = \phi_E \end{cases} \quad \text{Eq 2-39}$$

Assessment of the scheme: it has conservativeness, boundness, and transportiveness but has first-order accuracy, resulting in inaccurate results. However, the scheme is recommended for better convergence.

2.3.11 Solution algorithms

Solution algorithms solve the discretized momentum equations for solving the pressure field to yield velocity components by using linear algebra. This chapter reviews the Semi-Implicit Method for Pressure-Link Equations (SIMPLE) and Pressure Implicit with Splitting of Operators (PISO), solving steady-state and transient solutions, respectively.

The SIMPLE algorithm initiates a guessed field to solve the discretized momentum equations (UEqn.H), correcting the pressure field before adjusting the pressure and velocities (pEqn.H) and solving the transport equations (turbulence->correct()). The feedback loop adjusts the pressure and velocity until convergence, shown in Figure 2-11.

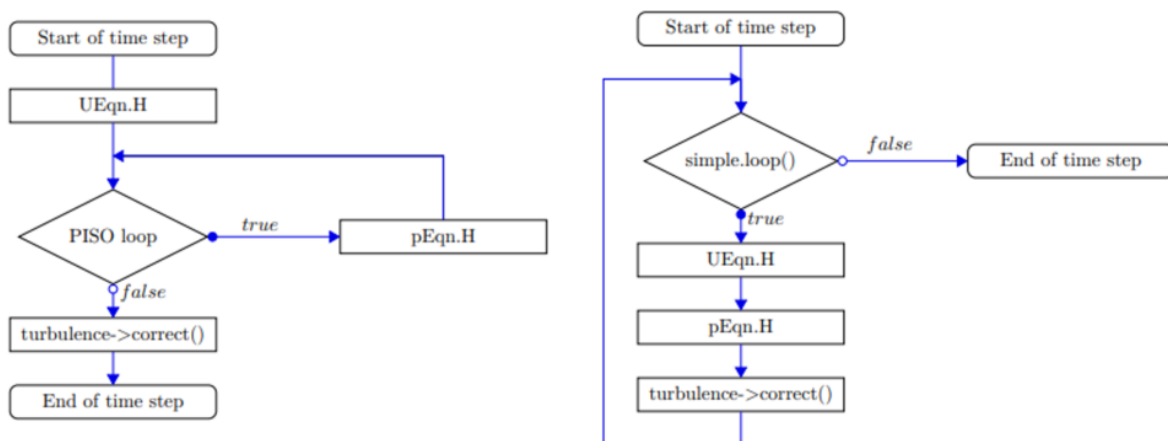


Figure 2-11: Flow chart of the PISO (left) and SIMPLE (right) algorithms [25]

PISO algorithm solves the discretized momentum equation once to solve the pressure and velocities corrector loop until the pressure equation converges.

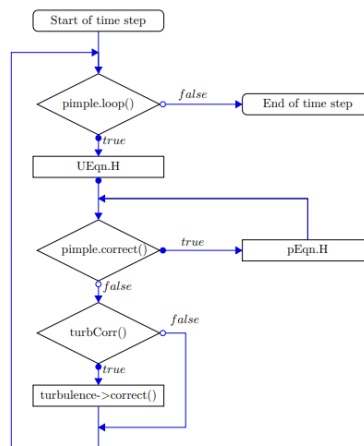


Figure 2-12: PIMPLE algorithm [25]

PIMPLE algorithm is a combination of SIMPLE and PISO, for solving large time-step for incompressible flow. The algorithm contains one extra loop for the turbulence correction.

2.4 Mesh

The mesh quality is an important aspect of the accuracy of the CFD simulation and impacts the convergence, stability of the simulation, and the numerical solution. Ensuring convergence, simulation stability, and accuracy, different mesh designs will be described in this sub-chapter.

2.4.1 Mesh structures

The mesh structures can be divided into two different types, structured and unstructured mesh. [13]

The structured mesh follows a cartesian pattern, which normally generates quadrilaterals for a 2D mesh, and hexahedron cells for a 3D mesh, which have four and six neighboring cells, respectively. For calculation, the results are more straightforward and require less computation time and power. [27] [13]

For an unstructured mesh, the cell pattern is irregular, and the mesh cell normally consists of triangles for a 2D mesh and tetrahedral for a 3D mesh, which has an inconsistent number of neighboring cells. This makes the computation more complex and may require a more complex solver resulting in higher computation time and power. Over the years, computational software and power have improved to handle these types of meshes. [27]

These two types of mesh can be combined to create a hybrid mesh, containing normally tetrahedral and hexahedral for a 3D mesh. The advantage of this type of mesh is that it is used for complex geometries and is applicable for mesh containing refined mesh.

2.4.2 Mesh quality

A high-quality mesh is essential for faster and more stable computations. Knut Vaagsaeter and Prasanna Welahetti prove that OF is more sensitive to skewness in a mesh compared to AF for

gas to gas single-phase mixing. [28] Due to these discoveries, focusing on a high-quality mesh is essential.

2.4.2.1 Refined mesh

When computing with a mesh that needs a local refinement close to the walls to resolve the physical boundary condition, the refined mesh is introduced. The physical boundary layer needs to be within 0.99 boundary layer thickness for the refinement to be acceptable. These local refinements result in better convergence and accuracy of the solution close to the walls. There are two types of refined mesh, steep transition and smooth transition. Smooth transition close to the walls can result in coarse meshes in the center of the mesh if this is not specified. Smooth meshes at inlets and outlets can also result in unmatching cells if the structured mesh is used. [29]

2.4.2.2 Aspect Ratio

The aspect ratio (AR) describes the mesh spacing in x- and y-directions and can be defined using Eq 2-42. The aspect ratio is recommended to be within the range of $0.2 < AR < 5$, but for the important flow areas, a large aspect ratio mesh is not recommended, resulting in diverging results. [27]

$$AR = \frac{\Delta y}{\Delta x} \quad \text{Eq 2-40}$$

2.4.2.3 Skewness

Skewness describes the angle between the gridlines of the mesh, where the optimal angle is 90° (orthogonal), and it is desirable to have an angle between $45^\circ - 135^\circ$. If the skewness exceeds these values, the computational error increases, and there will be numerical instabilities. For the mesh close to the wall, it is necessary to avoid non-orthogonal mesh cells, including the inlets and outlets are recommended to be as close to 90° as possible. [27]

2.5 ANSYS FLUENT

AF is a commercial CFD solver with high license expenses compared to the open-source solver OpenFoam (OF). AF is a more user friendly due to GUI (Graphic user interface). It is then necessary to describe how AF handles buoyancy-driven flow compared to OF.

For calculating natural convection using AF, the initial density is computed by initial temperature and pressure values. The operating density is the key to solving the buoyancy-driven flow by manually specifying a value. The operating density is included in the body force term in the momentum equation, as shown in Eq 2-41.

$$(\rho - \rho_0)g \quad \text{Eq 2-41}$$

Continued, for solving with a pressure boundary, shown in Eq 2-42.

$$p'_s = p_s - \rho_0 g x \quad \text{Eq 2-42}$$

The energy equation is manually activated in the GUI [30].

3 Method

This chapter will describe the method of experimental measurements, solver creation for a small-scale version, and implement the solver into a full-scale model, first in 2D and then 3D. The 3D model is validated against experimental data and AF model.

3.1 Measurements

Measurements of the outlet velocity and temperature are required for the validation of the model. The location of the measurement points is 0.5m away from the floor level of the footbridge, on the top of the roof of the pot room, as shown in Figure 3-1.

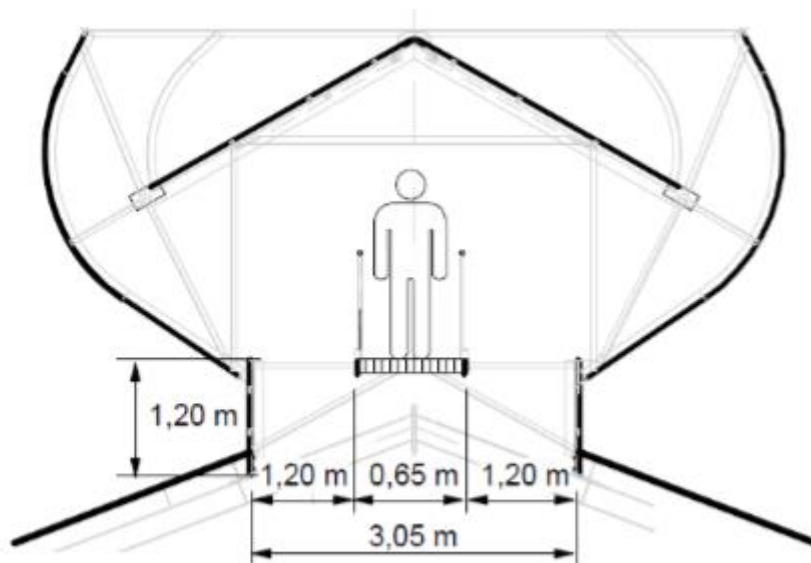


Figure 3-1 Ventilator at the top roof of pot room for C3

3.1.1 Temperature and velocity measurements

The temperature measurements were done using two temperature sensors (T8 and TC4, Figure 3-2) to determine ΔT , one for the outlet sampling and one for the environmental temperature inside the pot room. These temperature sensors are connected to a wireless system, Wisensys, and collected on a local computer. The sampling location is located below the left foot of the man, as shown in Figure 3-1. The inlet temperature data are collected from The Norwegian Meteorological Institute, which belongs administratively to the Ministry of Climate and Environment. [31]



Figure 3-2 - Temperature sensor T8 and TC 4

Velocity measurements are collected using TSI VelociCalc 9565-P. [32] The anemometer is calibrated every 12 months to ensure correct measurements by SINTEF. [Appendix B] Measurements are done by sampling over every second pot. Each measurement is done by holding the anemometer still for 30 seconds to check for variations. Repetitions on deviating measurements are done after the sampling to approve the measurements. The measured data are shown in Appendix C.

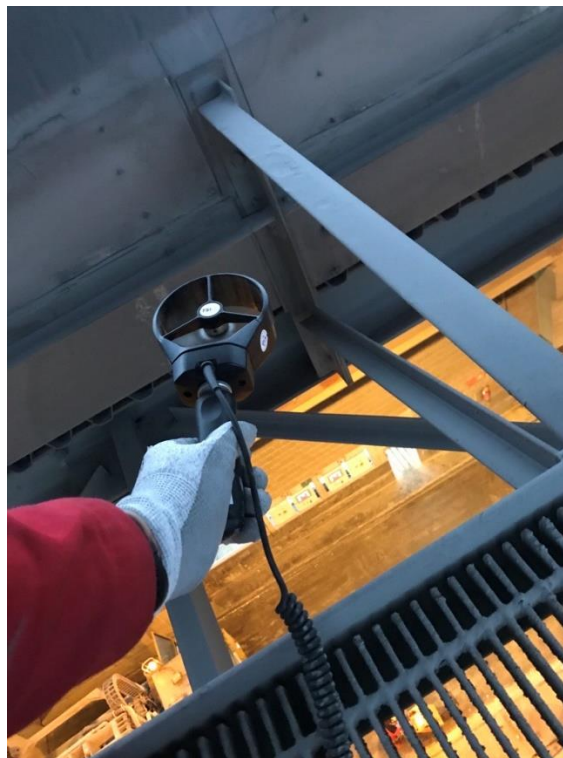


Figure 3-3 Velocity measurements

3.2 Solver

The solver is made first in a small-scale mesh and implemented in a full-scale model. The goal of the solver is to determine the estimated outlet velocity, temperatures, and flow pattern.

3.2.1 Small scale

The solver is a carryover from a mix of the heat-transfer tutorials in the OF folder. The mesh is created in a simpler mesh generator using blockMesh, using a maximum of 15 000 cells, with two inlets, an outlet, and one heated wall, simulating one small part of the pot room. The electrolysis cell is square for simplifications.

The Equation of State (EOS) is the ideal gas, noted perfectGas in OF. Boundary conditions are determined using the guideline from NEXTfoam to determine the correct boundary condition. [33]

The upwind scheme is chosen, for better convergence. [12] Solvers, sample functions and other optional functions are determined in the small scale.

3.2.2 Full-scale model

The full-scale mesh is made in AF and saved in ASCII format. Mesh conversions are done in the case file with the command *fluentMeshToFoam* for the 2D case and *fluent3DMeshToFoam* for the 3D case. Including inner walls, baffles are introduced, discussed in Chapter 4.4.3.

The solver is run multiple times to validate the model using the measurements. The results showcase the flow pattern and compare the temperature and mass flow with the measured data and calculated theoretical volume flow, as described in Chapter 2.3.3.

4 Preprocessing and Simulation

For this chapter, assumptions, the flow geometry, meshes for all cases, boundary conditions, the system and constant folder are represented.

4.1 Assumptions

- Incompressible ideal gas
- Adiabatic walls
- No-slip walls
- No porous zones

4.2 Mesh

The geometry of the meshes are described in this chapter.

4.2.1 Small scale

Three different meshes are used for the simulation cases and for the simulation of different scenarios, all created using blockMeshDict. BlockMesh is used to simplify and streamline the mesh.

4.2.1.1 2D “pot room”

Geometry similar to the pot room is created containing two inlets, one outlet, and one heated horizontal plate. For the full-scale version, the two inlets are one meter tall each, with a three-meter wide outlet. This geometric relationship is kept for the small-scale version with a mesh containing 14240 hexahedral. The outlet channel is set 10D lengths tall. The red patch in Figure 4-1 symbolizes the heated boundary layer. The full-scale version will not have this given outlet length, resulting in more unstable solutions.

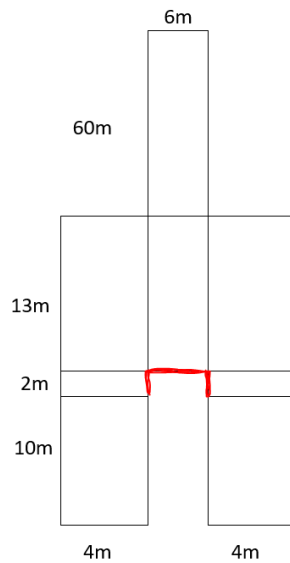


Figure 4-1: Geometry of the “small-pot”

4.2.1.2 With and without Refined mesh

Two meshes were created using blockMeshDict, both for a vertical channel divided into one inlet box, one heated box, and an outlet box with a height of 10m, 10m, and 60m, respectively. The middle box contains one heated wall with a heat flux of $3000\text{W}/\text{m}^2$, where the goal is to study the heat transfer close to the wall, with and without refined mesh. The boxes are five meters wide.

4.2.2 Full scale

The solver is implemented into an AF-generated mesh for 2D and 3D. The 2D model contains four inlets and two inlets, one outlet, and a heated zone, symbolizing the pot. The 3D model contains two inlets and one large elevated outlet patch. The model is decomposed and solved using a multiple processor computer and a cluster for the 2D and 3D models, respectively.

The geometry is given in the appendices of the technical drawings of the building. Drawings of the actual pot will not be given due to confidentiality, except a rough block drawing. Information is given in Appendix D. Visually, displayed in Figure 4-2, the small vents between the floor and the pot are not visible. For better details of the mesh, study Appendix G.

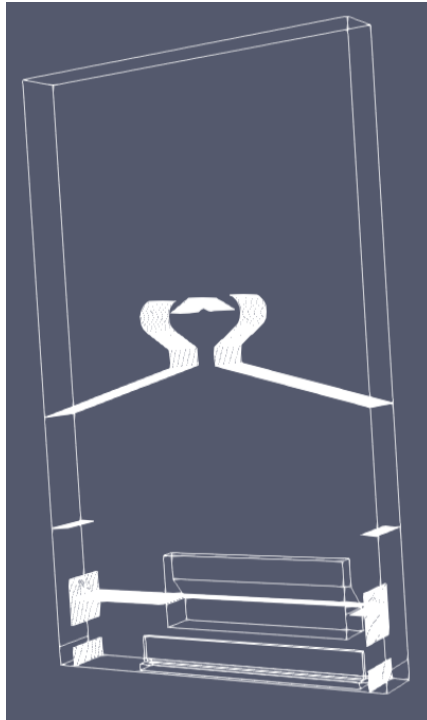


Figure 4-2 3D mesh of the pot room

4.3 Boundary conditions

Appropriate boundary conditions are important for the model to work. In this subchapter, the boundary conditions are divided into two due to correct validation for the 3D model. Overview of the 2D and 3D boundary conditions are shown in Table 4-1 and Table 4-2, respectively.

4.3.1 2D

For simplifications for both 2D models, the inlet velocity is fixed to 0.5m/s by a recommendation from Eirik Manger. [34] Darioush G. Barhaghi did similar measures for RANS and Large Eddy Simulations (LES) simulations cases for an HVAC case, setting inlet velocity to 0.6m/s to reduce temperature stratification due to recirculation. [11] The walls are assumed to have a no-slip condition while the outlet boundary condition is set to a fixed value for negative flux or equal to the neighbor cells for positive flux.

With respect to the airflow surroundings for the simulation cases, the inlet temperature is assumed to be 15°C. There is no insulation in the outer walls, but for simplification of the model, adiabatic boundary conditions are applied. Heat flux from the pot is given by using `externalWallHeatFluxTemperature`, where the heat flux values are from experimental data. These measured experimental data are classified and not specified.

Table 4-1: Boundary conditions for 2D models

2D	inlets	outlet	Heated walls	walls
alphan	calculated	calculated	compressible:: alphanJayatillekeWallFunction	compressible: :alphanJayatillekeWallFunction
epsilon	fixedValue	inletOutlet	epsilonWallFunction	epsilonWallFunction
k	fixedValue	inletOutlet	kqRWallFunction	kqRWallFunction
nut	calculated	calculated	nutUWallFunction	nutUWallFunction
p	calculated	calculated	calculated	calculated
p_rgh	fixedFluxPressure	totalPressure	fixedFluxPressure	fixedFluxPressure
T	fixedValue	inletOutlet	externalWallHeatFluxTemperature	zeroGradient
U	fixedValue	inletOutlet	no slip	no slip

The pressure is divided into two groups, hydrostatic (p) and dynamic pressure without hydrostatic pressure (p_rgh). The dynamic pressure at the outlet patch is controlled by the convective flux and the input entries. At the same time, the inlet, walls, and heated walls are controlled by the flux on the boundary, which is specified by the velocity boundary conditions.

4.3.1.1 3D

For the 3D case, inlet velocity is calculated by the neighbor cells or set to a fixed value equal to zero, depending on the flow direction. The heat flux is equal to the 2D case. The dynamic pressure has been rearranged to calculate the convective flux and input entries, while the outlet is changed to a generic outflow boundary condition.

Table 4-2: Boundary conditions for 3D models

3D	inlets	outlet	Heated walls	walls
alphan	calculated	calculated	compressible:: alphanJayatillekeWallFunction	compressible: :alphanJayatillekeWallFunction
epsilon	fixedValue	inletOutlet	epsilonWallFunction	epsilonWallFunction
k	fixedValue	inletOutlet	kqRWallFunction	kqRWallFunction
nut	calculated	calculated	nutUWallFunction	nutUWallFunction
p	calculated	calculated	calculated	calculated
p_rgh	totalPressure	inletOutlet	fixedFluxPressure	fixedFluxPressure
T	fixedValue	inletOutlet	externalWallHeatFluxTemperature	zeroGradient
U	outletInlet	inletOutlet	no slip	no slip

4.4 System

The system folder controls the domain with respect to time, discretizing schemes, solution algorithm, conjugate gradient solvers, and other optional functions. For this report, conjugated gradient solvers will not be discussed. Further information about these topics is explained in Weerstegen. [13]

4.4.1 ControlDict

ControlDict is setting the time variables, pressure-velocity coupling algorithms, and sampling functions. For the sampling function, writeObjects and surfaceFieldValue measure thermophysical variables across the domain and a specified location in the domain, respectively.

4.4.2 DecomposeParDict

DecomposeParDict is a directory file dividing the mesh into several parallel files, which utilizes the opportunity to run the simulation on several processor cores for decreased simulation time. For complicated geometries, the scotch decomposition is recommended, which requires no user input and optimizes for a minimum number of boundary processors.

4.4.3 creatBafflesDict

For internal walls, createBafflesDict creates infinite small walls in the domain, transforming internal faces into boundary faces.

4.5 Constant folder

OF 8 and OF v2112 (Version run in the cluster) vary slightly with the files structure, with the same parameter structure. For the turbulence properties, the file names are OF 9 and OF v2112 momentumTransport and turbulenceProperties, respectively.

4.6 Sampling and Plotting

For plotting, three different methods are used for sampling data. The first is the Plot over line function in ParaView, for plotting profiles over a line. For sampling variables over time, by utilizing surfaceFieldValue command in controlDict, the data are stored in the postProcess folder. The sampled data are gathered and saved into an LibreOffice Calc spreadsheet, where the data are converted to a more excel friendly format and later plotted.

For sampling the residuals, a new file is made, called resPlot. The resPlot file extracts logged data from the log-file data, which sample given variables residuals. For activating the logs file, use the command “application” > logs. This creates a logs file in the case file. The sampled residuals are the initial residuals, not the final residuals. Plot the sampled residuals in gnuplot with the command: load “resPlot”.

5 Results

The model base case is a copy from tutorial case files in the OF directory. The most relevant models, with inlet and outlet boundary conditions, are circuitBoardCooling and comfortHotRoom. Both use buoyantSimpleFoam, and comfortHotRoom uses Bousinessq approximation, which is selected as the EOS.

For visualization the ParaView 5.7.0 for OF 8 and ParaView 4.4.0 for OF v2112, are used to post-processing the 2D and 3D cases, respectively.

5.1 Experimental data

February and March proved to be windy, and the anemometer was only available between 15-17 March 2022. The 15th of March were the least windy day. Displayed by Table 5-1, experimental measurements were executed at 10:00 AM and 15:00 PM. Weather data for the noted data are sampled at seklima.met.no. The theoretical estimations prove that the volumetric flow is not affected by the environmental temperatures, meaning the velocities only vary by the wind. The measured data are expected to be higher than on a windless day.

Table 5-1: Measured velocity [m/s] top of pot room

01.03.2022	10:00	15:00	
C56	0,95	0,65	
C58	0,8	0,94	
C60	1,25	1,62	
C62	1,03	1,16	
C64	1,5	1,45	
C66	0,85	1,15	
C68	0,32	0,25	
C70	1,46	1,03	
C72	1,12	1,36	
C74	1,21	1,04	
C76	1,25	1,36	
C78	1,3	1,23	
C80	0,76	0,96	
C82	0,4	0,38	
U_averageIF>0.5m/s	1,12	1,16	1,143
Volume flow	20,22	20,93	20,573

Measured velocity differences are observed due to obstacles, larger floor area at the end of each section, and gusty wind. Consequently, the average of the measured data only includes measurements larger than 0.5m/s. This gives an average measured velocity of 1.143 m/s, and an average volumetric flow rate of 20.573 m³/s.

Previous measurements done at KTP and AP18 by other teams suggest a volumetric flow rate of 18.4 m³/s, meaning wind affects the flow rate.

The temperature measurements equipments haven't been working properly the last year, but a E.Manger recommend a temperature difference between the inlet and outlet temperature to be 15-20 degrees.

5.2 2D cases

The model cases are divided into three cases, one using the buoyantSimpleFoam in the simple geometry and buoyantPimpleFoam for small-scale and full-scale models.

5.2.1 Small scale

For time-saving, a steady-state solver using the Boussinesq approximation was considered. During the setup for the simulations, the model constantly crashed. In later stages, the model proved to simulate high surface temperature. Therefore, the Boussinesq approximation is not valid for the given turbulence model due to the dependency of linear temperature. The large surface temperature results are illustrated in Chapters 5.2.2 and 5.3.

The model was changed to the incompressible ideal gas EOS, where pressure differences drive the buoyancy forces due to stack effect and density change.

5.2.1.1 Steady-state vs pseudo-steady-state

The model continued in buoyantSimpleFoam in the "small-pot" geometry. The model proved not to be stable and kept crashing. A simpler version where made, shown in Figure 5-3, to check the boundary conditions. This proved to be working, and a further investigation of the "small-pot" geometry needed further investigation.

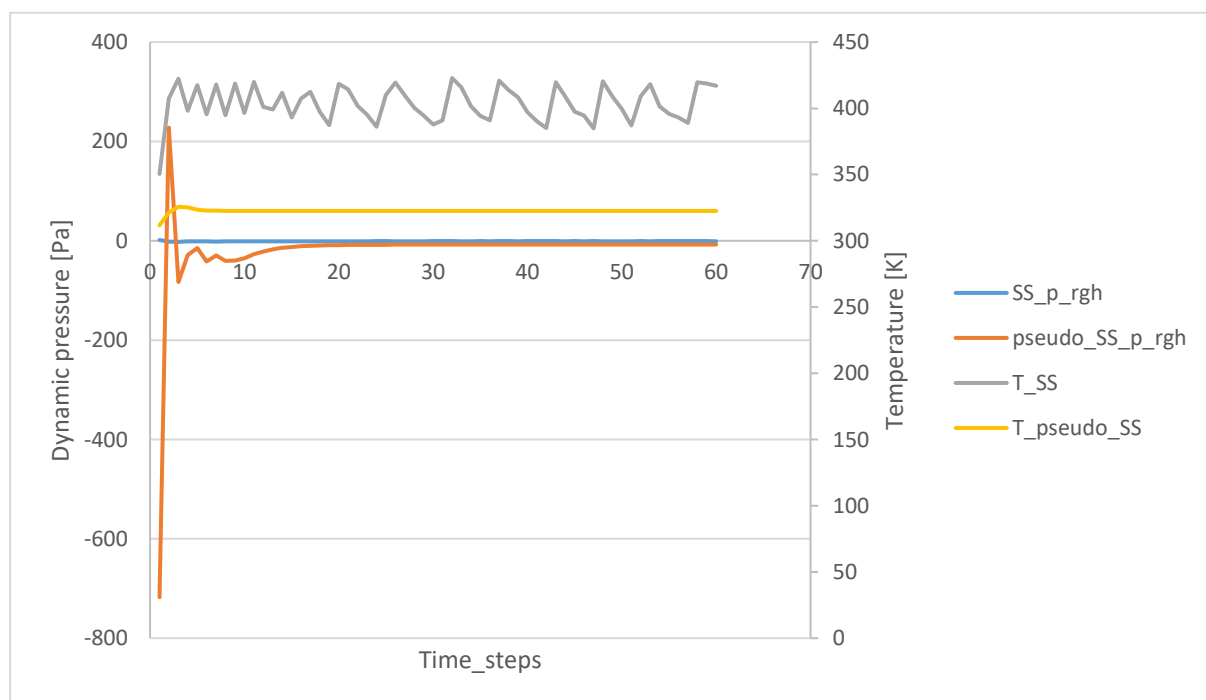


Figure 5-1: steady state vs pseudo steady state measured 0.4m from heated boundaries

When investigating 0.4 meters from the heated boundaries, the simulation proved to be pseudo-steady-state. As displayed in Figure 5-1, the initial dynamic pressure oscillations is monumentally more significant for the pseudo-steady-state model, “small pot” mesh (Figure 5-2), compared to the steady-state case, simple mesh (Figure 5-3). The temperature differences are not severe enough to affect the mass flow rate, proving the buoyantSimpleFoam cannot handle these pressure differences over time, with an almost stable mass flow rate.

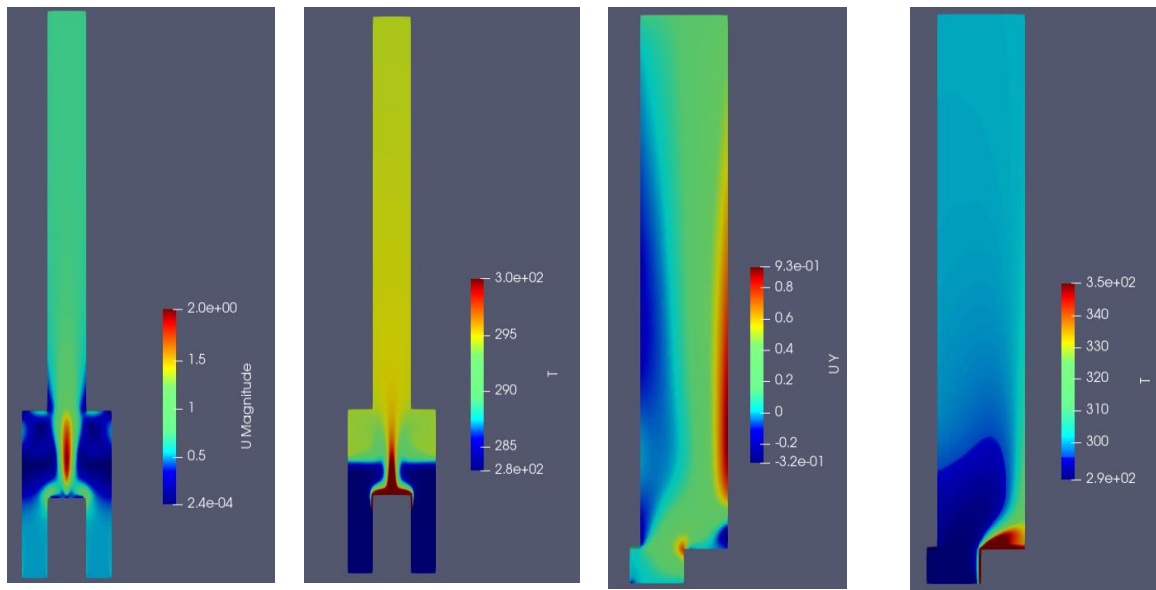


Figure 5-2: Pseudo-steady-state, "small pot" geometry

Figure 5-3: Steady-state, simple geometry

Other observations of both models are high surface temperatures. The surface area are small, due to 2D mesh. Further investigation in the full scale 3D, to address the problem.

5.2.2 Large scale

A comparison of the OF and AF models is carried out. For the turbulence models, the AF uses the $k-\omega$ model, and OF uses the $k-\epsilon$ model. The goal of the OF model is to reach similar temperature and mass flow outlet measurements compared to the AF model. Only pictures of the AF model are provided, and the comparable data will contain errors. Due to these predicted errors, the average measured data in the OF model are monitored at the outlet patches instead of the sampling location, as described in Chapter 3.1.1. The outlet patch area is 2.25 m², while the area for the sampling location is 3 m².

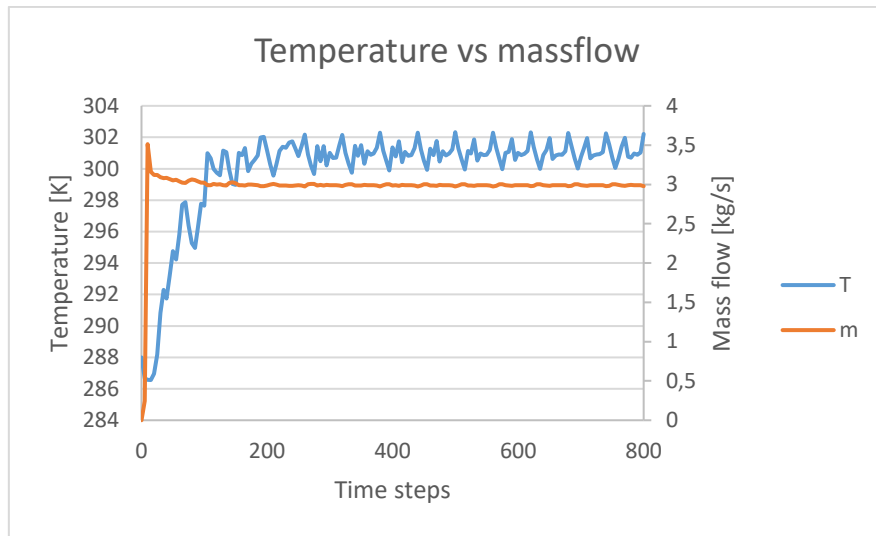


Figure 5-4 OF simulation of 2D large scale, with respect to temperature and mass flow

The AF model converged, with difficulties, due to a high number of degrees, while the OF model did not converge. [34] Natural convection is proven unstable, which can be shown in Figure 5-4. The model normalizes, but the temperature oscillations are still a problem. This can be due to the outlet patch being close to the heat source, and the 10D length rule is implemented in the geometry. [13]

Heat transfer close to the walls is proven better for the AF model compared to the OF model, as shown in Appendix E and F. The surface temperature reaches 1800K and 6200K for AF and OF model, respectively. The high surface temperatures are still due to the low surface area and have to be investigated in the large-scale 3D model.

5.2.3 Winter vs summer

Temperature variations between summer and winter vary between -15 degrees to 30 degrees (worst case). Due to these environmental changes, two simulations with different temperatures (268 and 288K) are analyzed. Theoretical estimations are described in Chapter 2.3.3 for validation of environmental temperature changes. The average collected data in Table 5-2 are between time steps 300-800.

Table 5-2: mass and volume flow rate differences between summer and winter

	T_{inlet}	T_{outlet}	$T_{\Delta T}$	$\dot{m} \left[\frac{kg}{s} \right]$	$\dot{V} \left[\frac{m^3}{s} \right]$
Winter	268	283,99	15,99	3,17	2,59
Summer	288	301,05	13,05	2,99	2,59
Difference	20	17,05	2,95	0,18	6,22E-05
%	6,94	5,67	18,42	5,98	0,0024

Model findings compared against theory shows the outlet mass flow increases by 5.98 percent between summer and winter, while the outlet temperature decreases by 5.67 percent, and the initial temperature decreases by 6.9 percent. For volumetric flow, the changes are neglectable

for the outlet patch. Another correlation is the temperature increase in the pot room between inlets and outlet. The temperature increases by 16 and 13 Kelvin for winter and summer, respectively.

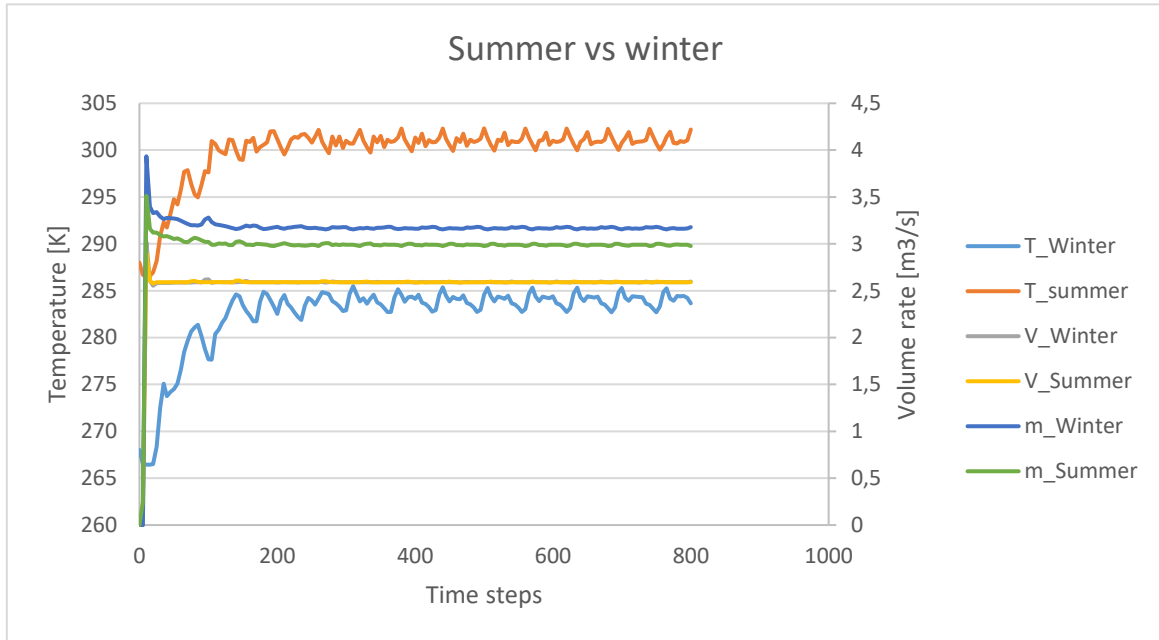


Figure 5-5: Winter vs summer

5.3 3D case

The full-scale model had minor changes for the constant folder to be compatible with the OF v2112 without changing the actual model. ParaView 4.4.0 is used for visualization. The sampling of the temperature and velocity profiles proved to be more primitive, creating more manual work compared to ParaView 5.6.0.

The standard $k-\epsilon$ model proved instabilities at the outlet resulting from changes in the flow direction. The late change to LRN $k-\epsilon$ stabilized the model, shown in Figure 5-6.

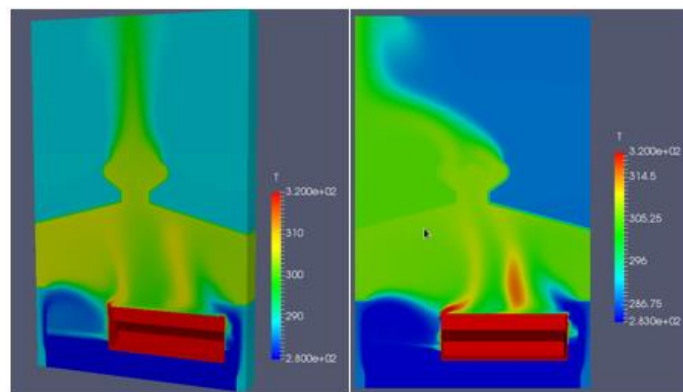
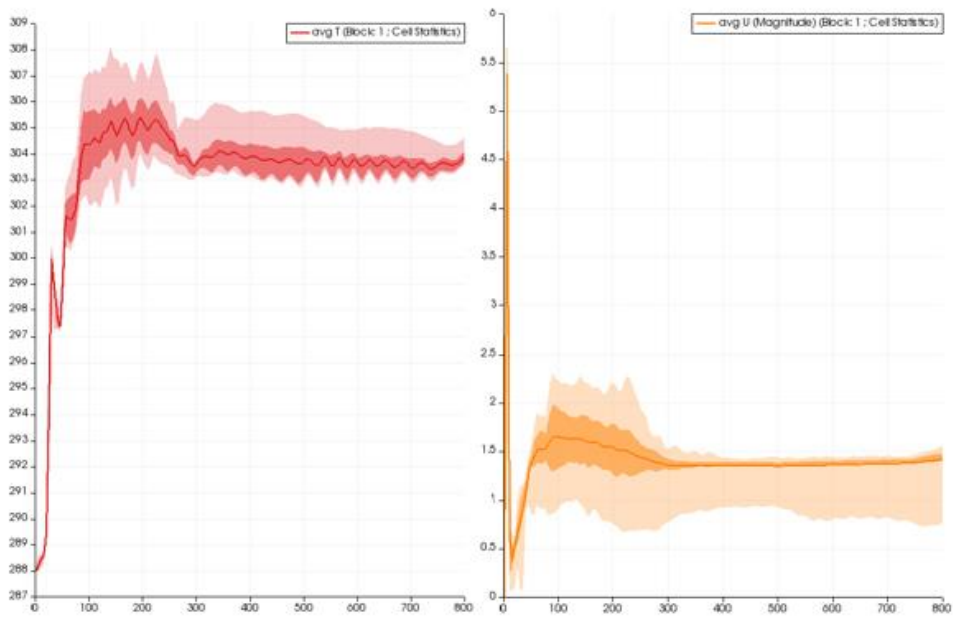


Figure 5-6: Flow structure of the LRN $k-\epsilon$ model (left) and standard $k-\epsilon$ model (right)



The model never converges but stabilizes. The modeled outlet temperature differences and velocity vary between 15-17K and 0.75-1.5 m/s, respectively. The dark line, the dark field, and the bright field show the average value, $\frac{3}{4}$ of the values and $\frac{1}{4}$ of the values, respectively. The temperature differences are within the experimental data range, but the average velocity has a 24.2 percent error. For the AF model, the volumetric outlet flow and temperature differences are 18.4 m³/s and 15K, respectively.

Table 5-3: Model data vs experimental

	deltaT	$u_{average} [\frac{m}{s}]$	$\dot{V}_{average} [\frac{m^3}{s}]$
OF-model	15-17	1,35	24,31
AF-model	15-20	1,02	18,4
experimental	15-20	1,02	18,44
error	Ok-	24,18	24,18

There are still high surface temperatures at the pot, which vary between 240 - 8864K. Temperatures below the pot are observed to be lower than inlet temperatures. Figure 5-7 shows buoyancy-driven flow below the pot with negative delta T in z-direction.

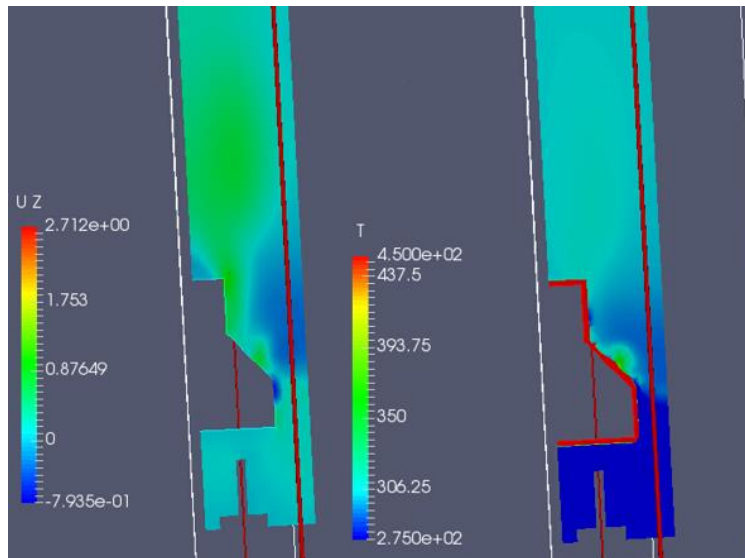


Figure 5-7: Temperature and velocity behavior close to the pot

The temperature and velocity behavior at the sides and top seems reasonable, creating a plume above the pot. The velocity profiles are correlatable to the literature for inclined and vertical plates, while temperature profiles occasionally have cold patches. [12] The temperature profile close to the pot has to be investigated later in this chapter. Above the floor, along with the pot, temperature stratification occurs and creates unstable flow. Circulation of flow in the pot room is observed, shown in Figure 5-8, caused by obstacles, displayed in Figure 4-2. The outlet patch is not stable due to backflow due to temperature stratification.

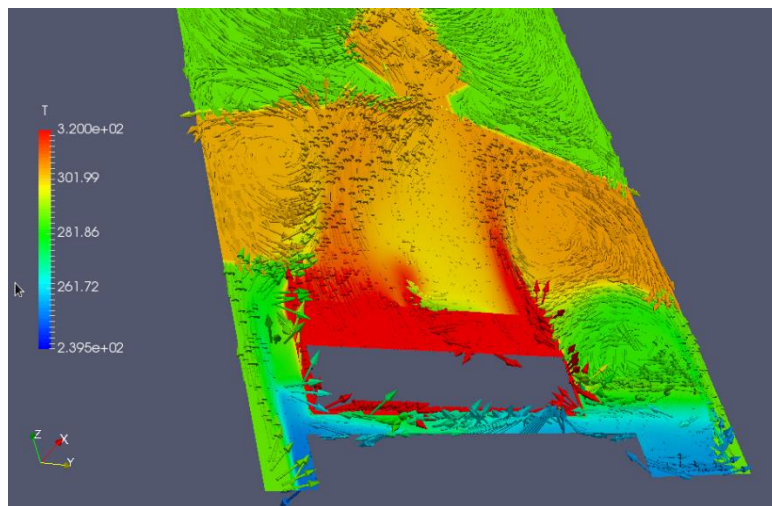


Figure 5-8: Flow pattern in the domain

Below the pot, there are observed negative temperature differences compared to inlet temperature. A late discussion with Erik Manger proved wrong heat flux at the bottom part of the pot. A late and improved simulation is shown in Figure 5-9. Further investigation of the outlet temperature and velocity is required.

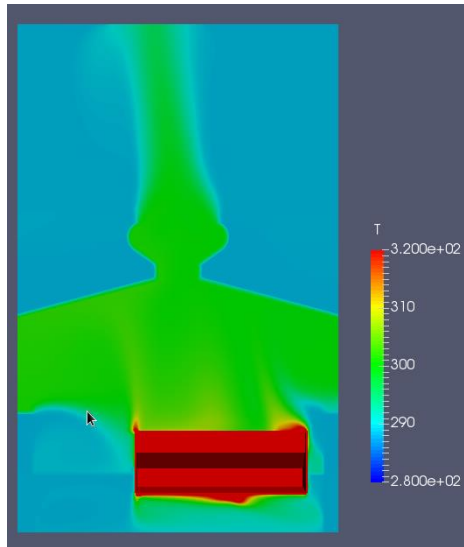


Figure 5-9: Increased heat flux at the bottom part of the pot

5.3.1 Location of the probe mounting

The goal of the thesis is to locate the location of the HF monitor. When studying Figure 5-10, The velocity out of the ventilator are almost uniform. Hence, the location seems higher on each side in the middle of the footbridge and the ventilator wall.

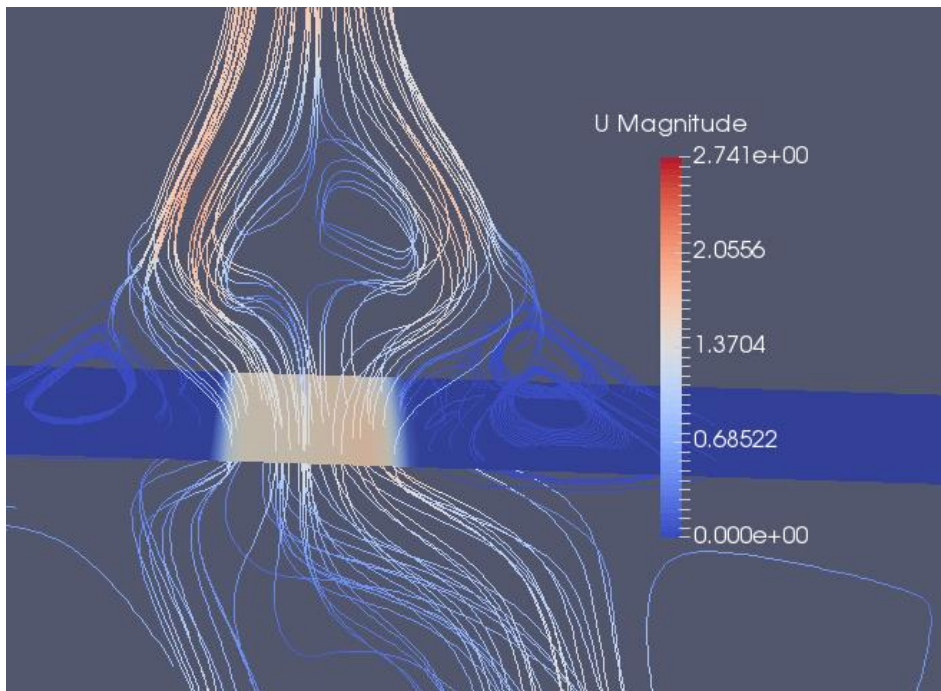


Figure 5-10: Streamlines of the flow through the ventilator, sampled 18m above ground

5.3.2 Mesh quality

Running the checkMesh function in Terminal returns skewness outside the acceptable range, resulting in computational errors. As described in Chapter 4.2, OF are sensitive to skewness. A closer study of the mesh, using the “Slice”-function in ParaView, prove low skewness close to the pot. Comparing Figure 5-11 and Figure 5-7 display energy not leaving cells due to poor mesh quality.

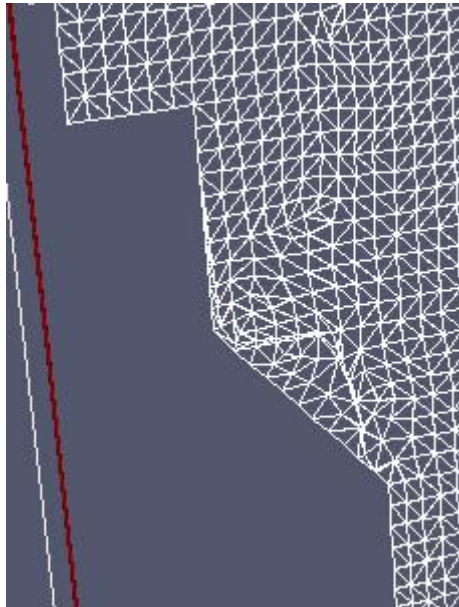


Figure 5-11: Poor mesh quality close to heated zones

By running the command `buoyantPimpleFoam -postProcess -func yPlus` in the Terminal, the log law proved to be close to acceptable for the model, displaying the y^+ in Table 5-4. Further investigation of the y^+ below 30 is necessary to determine the location in the mesh. Sampled y^+ data in Appendix I.

Table 5-4: y^+ values of the heated boundaries

y^+	Average	Min	Max
wall-pot-shell-bottom	67.79	29.86	81.45
wall-pot-shell-ends	45.13	21.62	74.48
wall-pot-superstructure	75.79	23.63	110.05

5.4 Mesh dependency

The mesh dependency needs to be determined, where the heat transfer for the transient $k-\epsilon$ solver is considered. The outlet and surface temperature are measured to determine if including refined mesh close to the pot will improve the total heat transfer of the model. The inlet velocity and heat flux are set to 1 m/s and 3000 W/m², respectively.

Table 5-5: Surface temperature with and without refined mesh

		q'' [W/m ²]	T_s [K]	T_{out} [K]
Mesh	30x30	3000	9879,28	287,006
Refined mesh	30x30	3000	2706,56	287,01
Improvement				0.001%

The outlet temperatures are equal, with and without refined mesh, while the local surface temperature decreases from 9879,28 K to 2706,56 K.

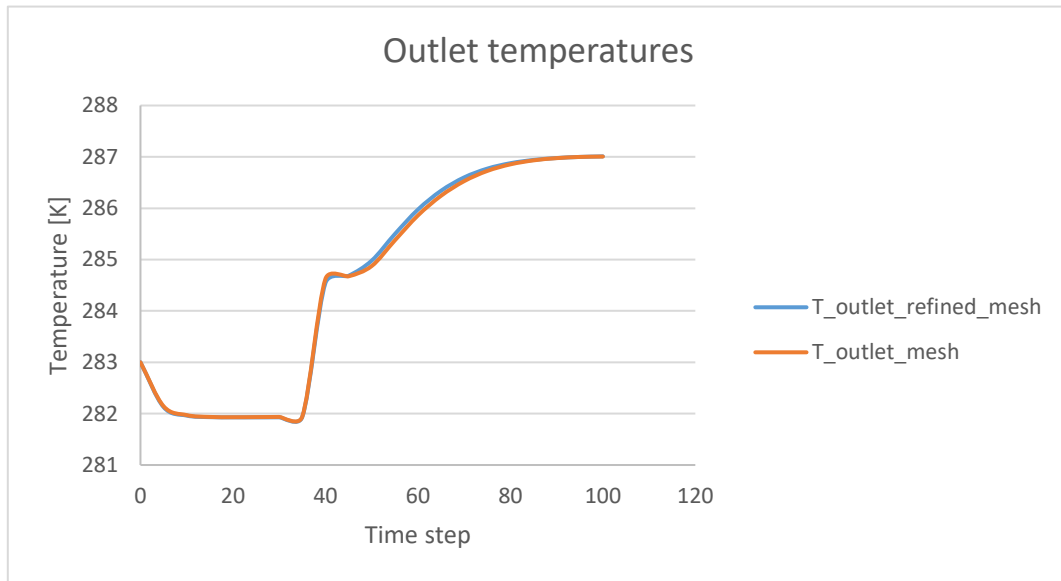


Figure 5-12: Outlet temperatures for the mesh study close to heated boundaries

6 Discussion

The Boussinesq approximation is not valid for the cases, proving all simulations having high surface temperature, which is not valid for the linear based temperature model. The buoyantSimpleFoam prove effective and time saving, but due to larger initial instabilities due to pseudo-steady-state results. By studying the SIMPLE algorithm, SIMPLE encounters instabilities due to the momentum equation for the SIMPLE algorithm. Changing to the PIMPLE algorithm, which is based on the PISO algorithm, solves the momentum equation once to solve the pressure and velocity until stability. When stable pressure differences, the momentum equation are calculated once again. This proves better robustness for a transient model, utilizing buoyantPimpleFoam.

For schemes, the upwind scheme was implemented for the natural convection model due to the convergence rate. The models never converge due to a high number of degrees of freedom. [34] With a closer look, all simulations prove to have temperature variations at the outlet. A further discussion of the schemes is further down in this chapter.

The full-scale 3D model proves to give correct streamlines in the domain, except below the pot, after a later discussion with E. Manger. [34] The heat flux at the bottom part of the pot and the boundary conditions on the ground floor have to be adjusted. A further investigation is needed for the boundary conditions below the pot due to positive buoyancy-driven forces, where the temperature differences are negative in the z-direction, studying Figure 5-7 and Figure 5-8. The last run with adjusted heat flux improved the temperatures below the pot, but observation of the outlet temperature and velocity relationship kept equal. For the outlet heated plume, the entering fluid from the quiescent region is observed, equal to the theoretical description.

Due to the obstacles in the domain, circulating flow occurs at both the top corners of the roof and the main floor. Discussing with E. Manger and comparing the result with studies of natural convection within enclosures with obstacles and various shapes, the flow circulation is valid, except below the pot floor. [34] [35] Further investigation is recommended for later work.

For the standard k- ϵ model, the outlet patch proved to be unstable at the outlet. A late change to the LRN k- ϵ model improved the stability at the outlet patch, proving the damping function of the transport model increases stability. For improving the LRN k- ϵ model, include Nagano (1990) damping functions and adjusted dissipations turbulent constants, developed for heat transfer. [22] Further, improving validation by further adjusting k and ϵ according to the equations in Chapter 2.3.7.1.

Another factor is the friction along the concrete walls located in the basement and lower part of the pot room due to porosity. AF has included the porosity, which is not included in the OF model. This is resulting in oscillating velocities between 0.7 and 1.6 m/s and averaging at 1.5 m/s for the OF model. Comparing with the experimental measurements, the outlet velocity is not valid. Including porous zones for concrete walls, will reduce the outlet velocity, hence improving the validation. To include porous zones, study the following OF tutorial by Chalmers (2009) with guidelines from the newer version of the OF (v2112) user guide. [36] [37] Porous zones will create more fluctuating flow, resulting in a more complex model in the pot room domain. The local complexity may affect the transport model since the outlet patch

is recommended to be moved further away for stable flow. Flow structure in the atmosphere suffers backflow due to density change, causing restructuring flow.

The walls in the pot room are adiabatic for further improving the model, including environmental temperature dependency at the walls, resulting in colder sides and density gradients of the pot room walls. This may affect the outlet temperatures.

For all cases when using heat flux, high surface temperatures occur. AF $k-\omega$ model proved high surface temperatures but not as severe as the OF model. There is no information about the AF model except the turbulence model. The OF model requires improved stability and more validation to be comparable with the AF model. Both models have higher surface temperatures than the experimental measurements, which are classified. Based on previous research, Jones and Launder suggested a LRN $k-\epsilon$ model using experimental data from forced convection. They predicted the flow within the viscous sublayer adjacent to the wall. [16] Further, To and Humphrey developed a model claimed to be developed for free convection. [38] Continued, Hanjalic and Vasic (1993) proved LRN $k-\epsilon$ improves the prediction of wall heat transfer, and later verified by Heindel (1994). [39] [40] Based on these studies, Davidson and Shia-Hui Peng (1999) used the LRN $k-\epsilon$ model and compared it with the $k-\omega$ model to predict the transitional boundary layer flow for natural convection flow in a tall cavity. Both models proved not able to produce grid independency solutions within the boundary layer. [4]

A further investigation of the model close to the heated walls can be investigated by using Large Eddy Simulations (LES). D.G. Barhaghi (2007) proved LES are valid close to the wall with and without radiation. Radiation heat transfer proved to be as high as 10% of the total heat flux. Therefore, the radiation heat transfer is recommended to be included in natural convection flow for the model to be valid close to walls. [11] Dimensionless analysis of Nusselt Number and Rayleigh Number close to the wall, and compare it with literature to validate the heat transfer close to the wall. [12]

The temperature changes are within 15-17K, which almost correlates with the experimental data (15-20K). Improvement of the convecting term in the momentum equation and the QUICK scheme has proven promising results. [23] [4] Weerstegen and Malalasekara discuss the stability of the scheme and prove the stability with correct conditions. The scheme has also proven to overshoot and undershoot the turbulent kinetic energy for the $k-\epsilon$ model in complex flow calculations. [13] For the model case, the QUICK scheme will improve the results closer to the wall. A recommendation is to change the geometry for the outlet patch when implementing the QUICK scheme. [37] [12]

Darcy's law can be applied to study the pressure loss and the concrete structure in the pot room. The theoretical calculations will never correlate with the simulations due to the complexity of the domain. For further work, including the porous zones will improve the correlations of the model.

The mesh quality of the domain has patches where the aspect ratio and skewness are not within the acceptable range, resulting in strange velocity and temperature profiles close to the pot wall. Due to this observation, the energy is not leaving the bad quality mesh, affecting the local environmental flow. The plume leaving the pot in Figure 5-7 would probably be wider due to the cold patch and poorly structured mesh, affecting the flow structure. The positive density gradient close to the plume causes recirculation and negative flow direction in the narrow vent between the floor and the pot. The $k-\epsilon$ may not be able to handle the narrow vent due to

rapid strain stress. Further investigation of the strain rate is necessary to determine the flow structure in the narrow vent by changing the RNG k- ϵ model. Continued, the study determines average y^+ to be acceptable. However, minimum computed values are below 30, which may disturb the flow. The y^+ reduces when the shear stress close to the wall increases. The expected minimum value for y^+ is believed to be located in the narrow vents, when analyzing Eq 2-38. For further work, confirming the location is essential to determine if the flow structure in the narrow vents is affected.

The refined mesh proved increased heat transfer close to the boundary, but the outlet temperature increase is neglectable. The results prove that refined mesh close to the heated boundary layers will not affect the outlet temperature, as confirmed by E. Manger. [34]

Comparing the OF and the AF is difficult because the information about the AF model is limited. However, Knut and Prasanna (2016) proved OF predicts higher diffusive and turbulent kinetic energy compared to AF. OF also required higher mesh quality. Due to the exploration of bad-quality mesh, the results can be uncertain. The AF model uses another mesh, which includes wind. Therefore the OF model needs further development to be comparable.

During the simulation for winter and summer, the theoretical validation proves the volumetric flow rate neglectable to temperature change. According to the result, the experimental data are only dependent on the wind. The temperature differences for winter and summer are not within the theoretical model and have to be further investigated in a validated 3D model.

When the wind is passing by the ventilator on top of the pot room, the increased velocity decreases the pressure, based on Bernoulli's Principle. The pressure drop at the outlet of the ventilator will elevate the level of the neutral pressure plane of the building and increase the inlet velocity, resulting in higher outlet velocity and higher emissions on a windy day. For later work, wind needs to be included in the model to study the effect on velocities in the pot room.

In the background of the results and the discussion, the location of the HF monitor has to be located in the middle of the ventilator wall and the footbridge, 18m above the ground floor. The footbridge and the small roof on top of the ventilator will obstruct the airflow. If the location of the probe is located at the footbridge, the measurements of the HF gas will be below the actual emissions. Bear in mind, the model is not validated and may deviate.

7 Conclusion

The thesis aimed to develop a physical model for natural convection on a small and large scale, determine the flow structure at the outlet of the pot room, and validate against experimental data and the AF model.

Measurements from the top of the roof of the pot room were collected and analyzed by a theoretical model and approved by the 2D full-scale model to establish the local velocity and temperature differences. By utilizing technical drawings of the pot room available by Hydro Aluminium Karmøy, a 2D and 3D mesh of the pot room was created in AF.

The simulation presents an open-source code called buoyantPimpleFoam based on the OF platform. A 2D small scale was created as the base model, with proven instabilities of the Boussinesq approximation due to high surface temperatures. Another Equation of State was required. Implementing an incompressible ideal gas for an unsteady state in the small scale model and later in the full-scale 2D and 3D model. For modeling the effect of turbulence, the buoyancy corrected standard k-epsilon and LRN models were employed. The standard k-epsilon model proved to be unstable for the outlet patch with the unsteady flow, which the LRN k-epsilon model stabilized due to the damping functions.

The simulations proved high surface temperatures for the small scale, 2D, and 3D large-scale models. The LRN k-epsilon model was not able to simulate the heat transfer close to the wall with the given mesh. A further study of refined mesh on heated boundary layers proved decreased surface temperature, concluding the outlet temperature is not dependent on heated refined mesh boundary layers.

The OpenFOAM model correlates outlet temperatures with experimental data and the ANSYS FLUENT model, while the outlet velocity proved wrong. The model is not fully developed due to irregular thermophysical properties below the pot, and porous zones are not included for concrete walls. A fully developed model will decrease the outlet velocities, improving the validation.

It is impossible to compare OpenFOAM and ANSYS FLUENT models due to the two different meshes and the underdeveloped OpenFOAM model.

The location of the HF monitor is recommended to be located in the middle between the wall and footbridge, 18m above ground floor. The roof on the ventilator and the footbridge obstructs the air, and may cause lower measurements compared to actual HF gas emissions.

7.1 Further work

- Apply non-adiabatic wall conditions to render the heat loss through the walls
- Implement porous zones in the model for increased pressure loss in the model.
- Further validation of the model
- Fix the mesh where the skewness and aspect ratio are outside the acceptable range.
- Elevate the outlet patch in z-direction for improved results
- Improving the modelling close to the wall by including LES and radiation.

References

- [1] A. N. Enviroment, "Agency Norwegian Enviroment," 2020. [Online]. Available: <https://www.norskeutslipp.no/en/Miscellaneous/Company/?CompanyID=5121>. [Accessed March 2022].
- [2] W. d. Gids, "Calculation method for natural ventilation of buildings.," TNO Research Institute for Enviromental Hygiene, Delft, Netherlands, 1979.
- [3] E. C. A. J. A. B. B. B. e. a. G. Desrayaud, "Benchmark solutions for natural convection flows in vertical channels submitted to different open boundary conditions," *International Journal of Thermal Sciences*, vol. 72, pp. 18-33, 2013.
- [4] ., L. D. Shia-Hui Peng, "Computation of turbulent buoyant flows in enclosures with low-Reynolds-number k-x models," *International Journal of Heat and Fluid Flow*, vol. 20, pp. 172-184, 1999.
- [5] EUR-Lex, "establishing best available techniques (BAT) conclusions, under Directive 2010/75/EU of the European Parliament and of the Council, for the non-ferrous metals industries," *Official Journal of the European Union*, June 2016.
- [6] Miljødirektoratet, "Tillatelse til virksomhet etter forurensningsloven for Hydro Aluminium Karmøy," 04 December 2015. [Online]. Available: https://nettarkiv.miljodirektoratet.no/hoeringer/tema.miljodirektoratet.no/Documents/Nyhetsdokumenter/hydroaluminiumkarmoy_tillatelse041215-2.pdf. [Accessed 23 March 2022].
- [7] S. K. S. C. Andrew R.Hinda, "The surface chemistry of Bayer process solids: a review," *Colloids and Surfaces A: Physicochemical and Engineering Aspects*, vol. 146, no. 1-3, pp. 359-374, 1999.
- [8] R. M. & H. A. Arne Petter Ratvik, "Aluminium production process: from Hall-Héroult to modern smelters," *ChemTexts* 8, 2022.
- [9] S. Prasad, "Studies on the Hall-Heroult Aluminum Electrowinning Process," *Journal of the Brazilian Chemical Society*, vol. 11, 2000.
- [10] S. C. S. a. A. Hossain, "Natural Convection Flow With Combined Buoyancy Effects due to Thermal and Mass Diffusion in a Thermally Stratified Media," *Nonlinear Analysis*, p. 101, 2004.
- [11] D. G. BARHAGHI, "A Study of Turbulent Natural Convection Boundary Layers Using Large-Eddy Simulation," CHALMERS UNIVERSITY OF TECHNOLOGY, Goteborg, Sweden, 2007.
- [12] D. P. D. T. L. B. A. S. L. Frank P. Incropea, *Incropea's Principles of Heat and Mass Transfer*, vol. 8th, John Wiley & Sons Singapore Pte.Ltd, 2017.

- [13] H. V. a. W. Malalasekera, An Introduction to Computational Fluid Dynamics, second ed., Harlow: Pearson Education Limited, 2007, pp. 162-163, 285-301, 304-315.
- [14] D. D. a. AldoGiorgini, "The validity of the boussinesq approximation for liquids and gases," *International Journal of Heat and Mass Transfer*, vol. 19, no. 5, pp. 545 - 551, May 1976.
- [15] A. Bhatia, "HVAC – Natural Ventilation," CED Engineering, Woodcliff Lake.
- [16] J. W. a. L. B. E, "The Prediction of Laminarization with Two-Equation Model of Turbulence," *Int J. Heat Mass Transfer*, vol. 15, pp. 301-314, 1972.
- [17] R. K. a. A. Dewan, "URANS computations with buoyancy corrected turbulence models for turbulent thermal plume," *International Journal of Heat and Mass Transfer*, vol. 72, pp. 680-689, 2014.
- [18] B. a. S. D. Launder, "The numerical Computation of Turbulent Flows," *Computer Methods in Applied Mechanics and Engineering*, vol. 3, pp. 269-289, 1974.
- [19] A. J. H. G. & A. D. G. R. W. Benodekar, "Predicting lift-off of major self-heating releases under the influence of a building," *Safety of Thermal Water Reactors*, pp. 385-397.
- [20] K. V. M. a. B. Merci, "Application of two buoyancy-modified k-ε turbulence models to different types of buoyant plumes," *Fire Saf. J*, vol. 41, pp. 122-318, 2006.
- [21] Z. Z. H. L. M. L. a. J. X. Xin Nie, "A comparative study of heat transfer characteristics of wall jet with boundary layer transition using six low-Reynolds number k-ε models," *AIP Advances*, vol. 11, 2021.
- [22] M. T. Y. Nagano, "An improved k-ε Model for Boundary Layer Flows," *Journal of Fluids Engineering*, vol. 112, pp. 33-39, 1990.
- [23] C. Suvanjumrat, "Implementation and Validation of OpenFOAM for Thermal Convection of Airflow," *Engineering Journal*, pp. 231-237, 2017.
- [24] W. a. L. B. Jones, "The prediction of laminarization with a two-equation model of turbulence," in *Heat Mass Transfer*, vol 15, 1972, pp. 301-314.
- [25] G. Holzinger, "OpenFOAM, A little User-Manual," 27 January 2016. [Online]. Available: <https://www.cfd-china.com/assets/uploads/files/1621928562433-openfoam-user-manual-pfm.pdf>. [Accessed March 2022].
- [26] A. B. Donald A. Nield, Convection in Porous media, Cham: Springer International Publishing : Imprint: Springer, 2017, pp. 3-5, 175-183.
- [27] G. H. Y. a. C. L. Jiyuan To, Computational Fluid Dynamics : A Practical Approach, Melbourne: Elsevier Science & Technology, 2018, pp. 127, 133, 149-150.

- [28] K. V. Prasanna Welahetti, "Computational Fluid Dynamic Simulation of Gas-Gas Single Phase Mixing with and without Static," Department of Process, Energy and Environmental Technology University College of Southeast Norway , Porsgrunn, Norway .
- [29] H. Jasak, "Error Analysis and Estimation," Department of Mechanical Engineering Imperial College of Science, Technology and medicine, London, 1996.
- [30] A. inc, "ANSYS Fluent Tutorial Guide," Ansys.inc, January 2017. [Online]. Available: <http://www.ansys.com>. [Accessed April 2022].
- [31] T. N. M. Institute, "Meteorologisk institutt," [Online]. Available: <https://www.met.no/en>. [Accessed 22 03 2022].
- [32] TSI, "tsi.com," TSI, [Online]. Available: <https://tsi.com/products/ventilation-test-instruments/multi-function-ventilation-meters/velocicalc-multi-function-ventilation-meter-9565/>. [Accessed 17 March 2022].
- [33] N. foam, "NEXT foam, Boundary Conditions - OpenFOAM-4.1," May 2017. [Online]. Available: <https://nextfoam.co.kr/>. [Accessed 2 February 2022].
- [34] E. Manger, Interviewee, *Personal Communication*. [Interview]. February-May 2022.
- [35] M. R. T. B. Debayan Dasa, "Studies on natural convection within enclosures of various (non-square) shapes – A review," *International Journal of Heat and Mass Transfer*, vol. 106, pp. 356-406, 2017.
- [36] H. E. Hafsteinsson, "tfd.chalmers.se," 2009. [Online]. Available: http://www.tfd.chalmers.se/~hani/kurser/OS_CFD_2008/HaukurElvarHafsteinsson/haukurReport.pdf. [Accessed 10 05 2022].
- [37] O. Ltd., "OpenFOAM: User Guide v2112," OpenCFD Ltd., 2021. [Online]. Available: <https://www.openfoam.com/documentation/guides/latest/doc/index.html>. [Accessed February 2022].
- [38] J. A. C. To W. M. and Humphrey, "Numerical Simulation of Buoyant Turbulent flow-I, Free Convection Along a Heatedd, Vertical Flat Plate," *Int. J. Heat and Mass Transfer*, vol. 29, pp. 573-591, 1986.
- [39] S. V. Kemal Hanjalić, "Computation of turbulent natural convection in rectangular enclosures with an algebraic $\bar{u}x$ model," *International Journal of Heat and Mass Transfer*, vol. 36, pp. 3603-3424, 1993.
- [40] S. R. F. P. I. T. J. Heindel, "Assessment of turbulence models for natural convection in an enclosure," *Numerical Heat Transfer*, vol. 26, pp. 147-172, 1994.
- [41] D. G. BARHAGHI, "A Study of Turbulent Natural Convection Boundary Layers Using Large-Eddy Simulation," CHALMERS UNIVERSITY OF TECHNOLOGY, Goteborg , Sweden, 2007.

Nomenclature

Appendices

Appendix A: Master's Thesis Description

Appendix B: Calibration certificate of TSI 9565 – P, Pressure and velocity.

Appendix C: Expérimental data

Appendix D: Building Geometry

Appendix E: 2D OpenFOAM

Appendix F: 2D ANSYS FLUENT

Appendix G: 3D OpenFOAM

Appendix H: 3D ANSYS FLUENT

Appendix I: y^+ measurements for 3D model

Appendix A: Task Description



www.usn.no

FMH606 Master's Thesis

Title: CFD analysis of airflow in pot room

USN supervisor: André Vagner Gaathaug, Prasanna Welahettige

External partner: Hydro Karmøy, Eirik Manger

Task background:

Reduction of fluoride emissions over roof from pot room is prioritized at Hydro Karmøy, both in AP18 and at KTP. While KTP has emissions under control, AP18 has seen a gradual increase in emissions over roofs in early 2021. The interplay between mechanical encapsulation of cells through good covers, collars, drain doors and the use of forced extraction, along with extraction volume and proper balancing of cells, forms the interface with gas purifier, the one that traps the exhaust gas from the electrolysis cells and therefore it is essential to keep the leakage area to a minimum.

Hydro is interested determining the flow structure in the pot room, to find the optimum location for the HF monitor. To solve this, an exact and robust CFD model is needed, which will be controlled by a FLUENT model, created by Erik Manger. By comparing these two models, we can determine the accuracy for OpenFOAM.

Task description:

Technology and Operational Support has already started evaluating the situation using Boreal HF laser and measured air velocity in the top of the pot room. The task will be to set up a model for one section in the pot room, containing 28 electrolysis cells, and evaluate the room to determine how the airflow moves. The main task for the project is:

- Literature review of relevant methods and results
- Development of physical model
- Validate the model using measured velocities data
- Compare the model with an existing FLUENT model

Student category: Process Technology

Is the task suitable for online students (not present at the campus)? Yes

Practical arrangements:

Hydro Karmøy and Eirik Manger will supply the required data.
The USN supervisor is expected to supervise the student 15-20 hours.

Supervision:

André Vagner Gaathaug, Prasanna Welahettige

Signatures:

Supervisor (date and signature)

13/5-22 

Faculty of Technology, Natural sciences and Maritime Sciences
Campus Porsgrunn

Appendix B



KALIBRERINGSBEVIS

Oppdragsfører:
Hydro Aluminium (KLS)
Karmøy Metallverk
N-4265 Håvik

Kontaktperson:
Ø. Matre, Sentrallager

Vår ref:
O 423/22-61084

Serienummer: P1408026 Fabrikat: TSI mod 9565-P [Pa]

Merknader:
Instrumentet ble ikke justert.

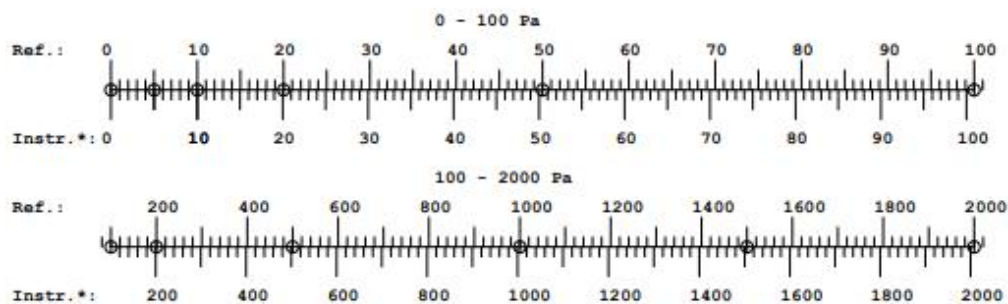
Instrumenttype:
MM

Eskild Svee Dahl
2022.01.19
125359+0100'

Neste kalibrering:
19.01.2023

Kal.dato:
19.01.2022 Kalibrert av:
ESD

Lufttemp. i lab.: 19,8 °C Luftfukt. i lab.: 30,8 %RH Barometerykk: 985,8 hPa



Referanse	Instrument	Korreksjon	Avlest
0,000	0,000	0,000	
5,00	5,00	0,00	
10,00	10,00	0,00	
20,00	20,10	-0,10	0 - 100 Pa
50,00	50,40	-0,40	
100,0	100,9	-0,9	
100,0	100,9	-0,9	
200,0	201,6	-1,6	
500,0	503,0	-3,0	100 - 2000 Pa
1000	1005	-5	
1500	1505	-5	
2000	2008	-8	



SPORBARHET

Barometer

Type: Coreci KC2585
Serienummer: 1153524
ID-nummer: 3724

Mikromanometer 0-2000Pa

Type: Furness PPC500
Serienummer: 0202012
ID-nummer: 3728

Temperatur- og luftfuktighetsføler

Type: Vaisala HMP233
Serienummer: R5120017
ID-nummer: 3732



KALIBRERINGSBEVIS

KALIBRERING FOR LUFTHASTIGHET

Oppdragsgiver:
Hydro Aluminium (KLS)
Karmøy Metallverk
N-4265 Håvik


Kontaktperson:
Ø. Matre, Sentrallager

Vår ref:
Ø 423/22-61083

Serienummer: P1408026 Fabrikat: TSI mod 9565-P [m/s]

Instrumenttype:
TA

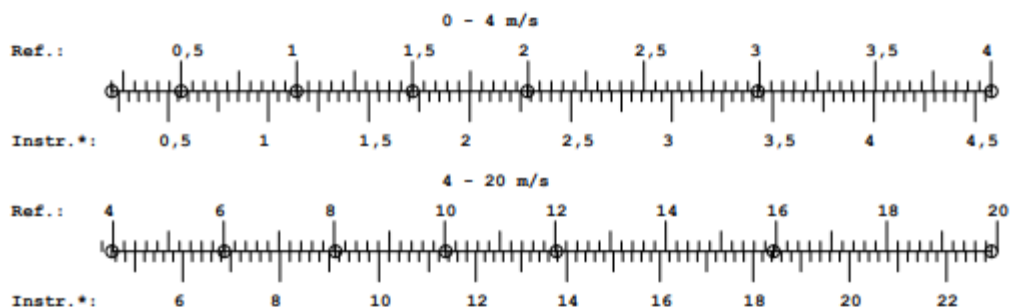
Merknader:
Middelavvik=14,4%
Maksavvik=15,6% v/15,95m/s
Instrumentet ble ikke justert.
Neste kalibrering:
19.01.2023

 Eskild Svee Dahl
2022.01.19
12:43:35 +0100'

Kal.dato: 19.01.2022 Kalibrert av: ESD

Kalibreringsverdiene gjelder
ved lufttetthet 1,2 kg/m³

Lufttemp. i lab.: 20,2±0,6 °C Luftfukt. i lab.: 27,8 %RF Barometertrykk: 986,1 hPa



Referanse	Instrument	Korreksjon	Avlest	
0,201	0,216	-0,014	0,21	
0,501	0,566	-0,065	0,55	
1,000	1,142	-0,142	1,11	
1,501	1,718	-0,217	1,67	0 - 4 m/s
1,997	2,284	-0,287	2,22	
2,993	3,427	-0,434	3,33	
4,002	4,580	-0,578	4,4	
3,978	4,519	-0,541	4,4	
6,01	6,87	-0,86	6,7	
8,02	9,13	-1,10	8,9	
10,02	11,34	-1,32	11,1	4 - 20 m/s
12,02	13,78	-1,75	13,4	
15,95	18,44	-2,49	17,9	
19,89	22,92	-3,03	22,3	

**SPORBARHET****Vindtunnel**

Type: SINTEFs vindtunnel

Serienummer: 3725

ID-nummer: 3725

Barometer

Type: Coreci KC2585

Serienummer: 1153524

ID-nummer: 3724

Temperatur- og luftfuktighetsføler

Type: Rotronic HF535-WE3XX13X

Serienummer: 61404396

ID-nummer: 3514

Temperatur- og luftfuktighetsføler

Type: Vaisala HMP233

Serienummer: R5120017

ID-nummer: 3732

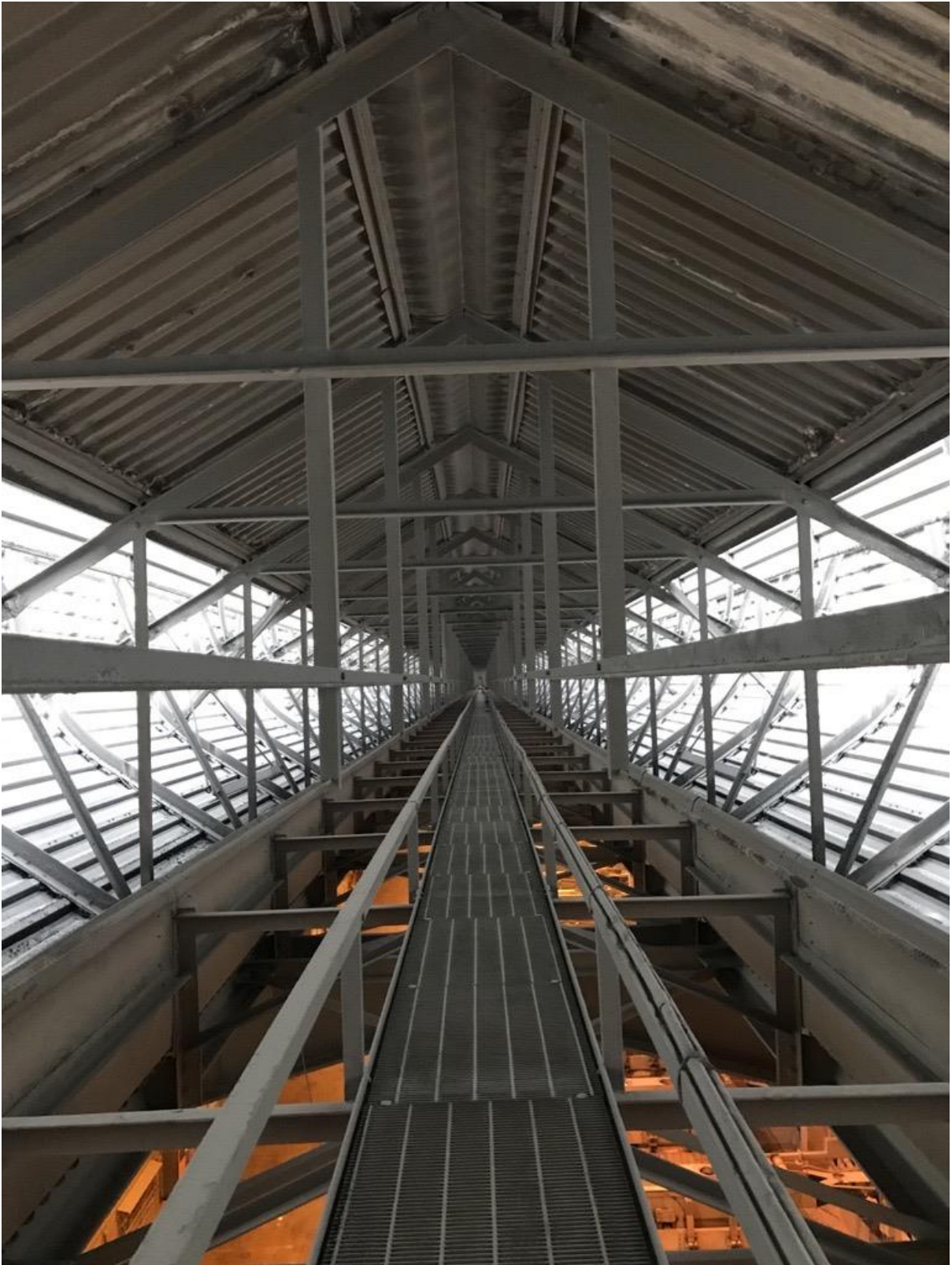
Appendix C Experimental data

Sampling from the ventilator. The measurements are varying, due to obstacles and floor at ends of each section

01.03.2022	10:00	15:00	
C56	0,95	0,65	
C58	0,8	0,94	
C60	1,25	1,62	
C62	1,03	1,16	
C64	1,5	1,45	
C66	0,85	1,15	
C68	0,32	0,25	
C70	1,46	1,03	
C72	1,12	1,36	
C74	1,21	1,04	
C76	1,25	1,36	
C78	1,3	1,23	
C80	0,76	0,96	
C82	0,4	0,38	
U_averagelF	1,12	1,16	1,143
Volume flow	20,22	20,93	20,573

Navn	Stasjon	Tid(norsk normalt)	Høyeste middelvind (døgn)	Høyeste middelvind fra hovedobs. (døgn)	Høyeste vindkast (døgn)	Laveste høye vindkast (døgn)	Laveste av høyeste middelvindverdier (døgn)				
Haugesund Lufthavn	SN47260	15.03.2022	9,3	7,7	13	5	3,8				
Data er gyldig per 12.05.2022 (CC BY 4.0), Meteorologisk institutt (MET)											

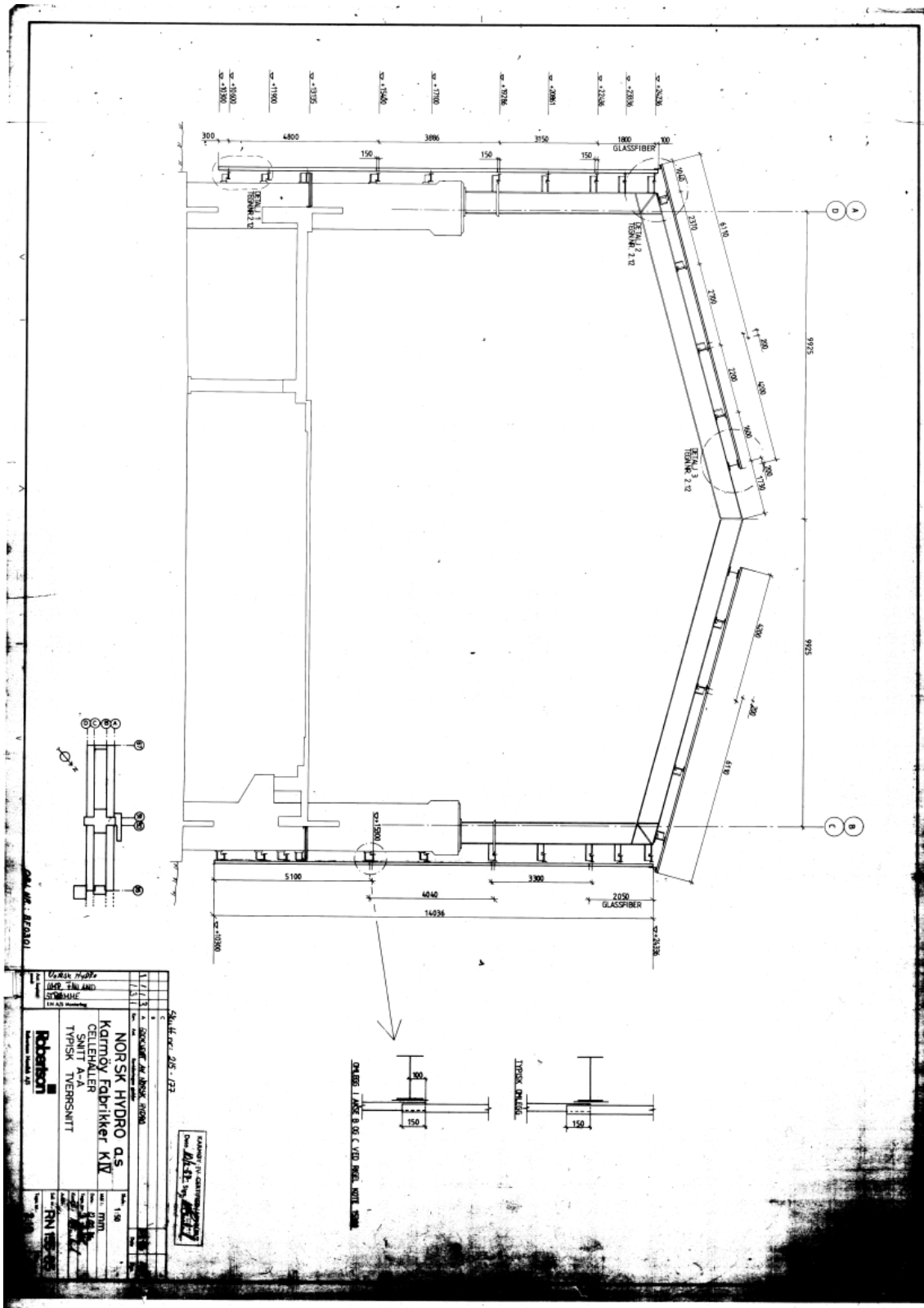


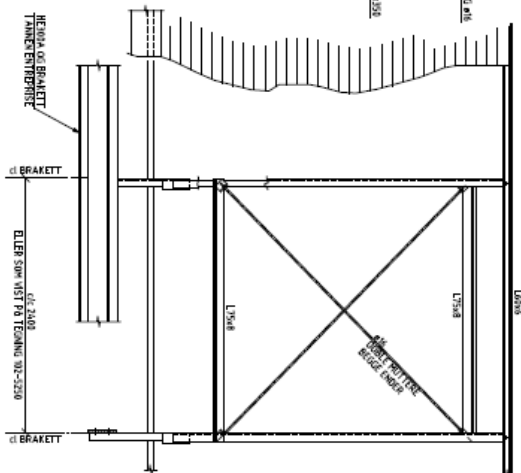
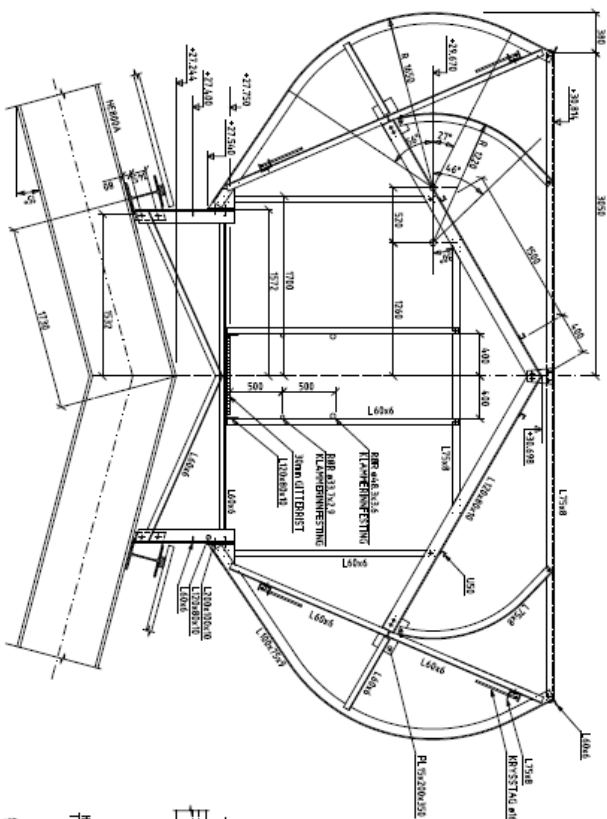




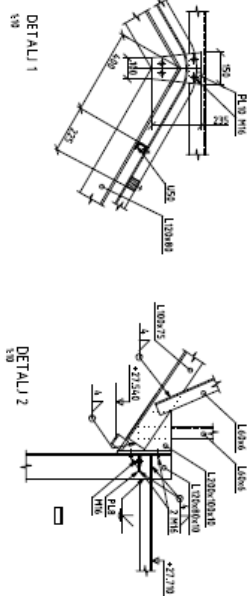


Appendix D: Building Geometry





TYPISK RANNE



FØRKLÆRINGER

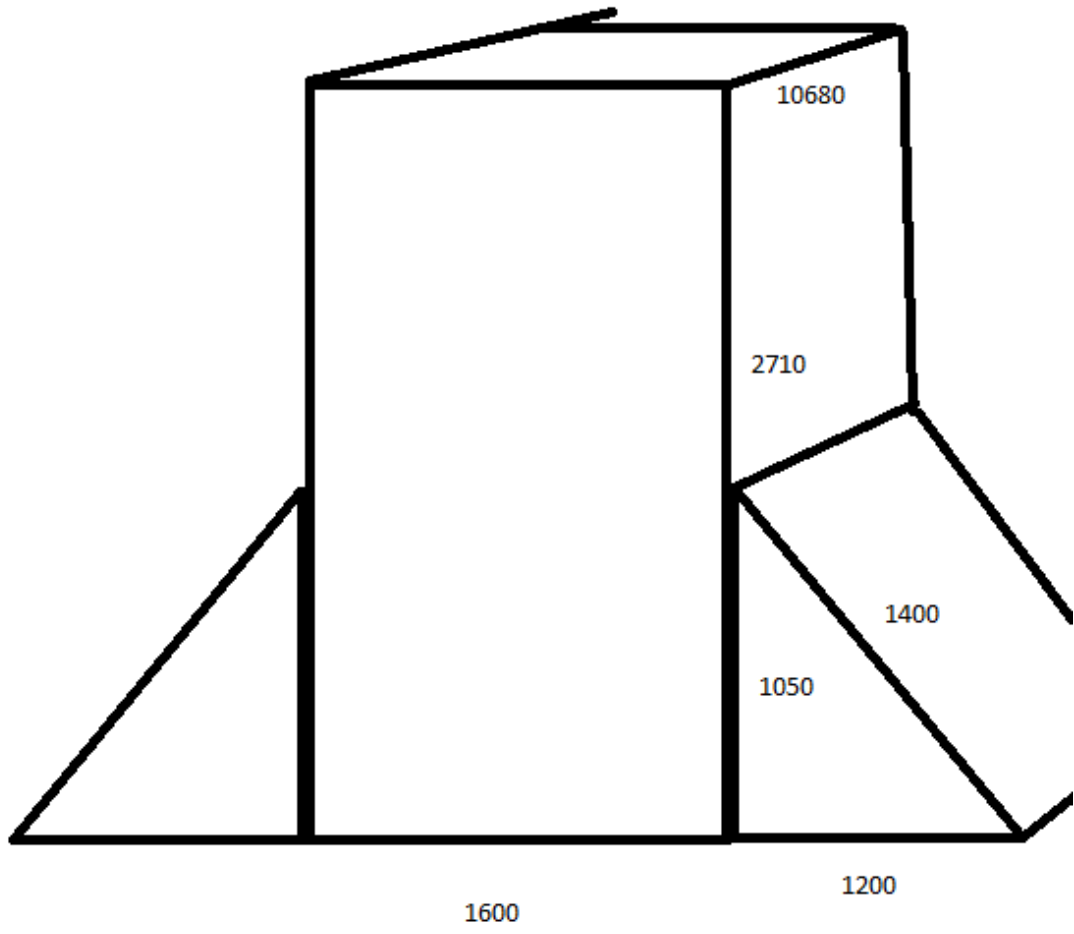
- BESTEMMELSER**
1. STANDARDE: NS 3471 DS NS 3470
 2. UTRUSTET: TILBÆRINGER NS 3471, TILBÆRINGER 2
 3. KOPTEL: TILBÆRINGER 2 OG 200 ANDET TILBØR BEHØRIG.
 4. MATERIALE: S 235 R OG HECHVALD TIL BINDEREN X
 5. SVRER: IBERGVALTUTLÆSERE, RENHOLD TIL NS 3470 ALLE SVRER (S) IBERGVALTUTLÆSERE ANDET. BYGGERIET ER ANVET FOR SVRER. VÆR KVALITET I BEREGNINGEN. BILDETS BRUK ER FØLGENDE ETTERFØRINGS OG BEREGNINGEN. HJERNETRE RINGELER (S) IBERGVALTUTLÆSERE ANDET.
 6. BYGGERIET: 2-ØPPROPPET SVRER HVALE 2000-200 HJERNETRE RINGELER (S) IBERGVALTUTLÆSERE ANDET.
 7. ØPPROPPET SVRER HVALE 2000-200 HJERNETRE RINGELER (S) IBERGVALTUTLÆSERE ANDET.
 8. ØPPROPPET SVRER HVALE 2000-200 HJERNETRE RINGELER (S) IBERGVALTUTLÆSERE ANDET.

HEMVISNINGER

- 02- 5070 VÅTTE KANE 50-51
5070 TYPISK RANNE
5071 TYPISK RANNE KANE 44-48/48-48
5072 TYPISK RANNE KANE 50-52/50-52
5073 TYPISK RANNE KANE 50-52/50-52
5074 TYPISK RANNE KANE 50A-8
5075 TYPISK RANNE KANE 50A-8
5076 ROR TYPISK DETALJ
5077 ROR TYPISK DETALJ
5078 KANALVÅY 14
5079 KANALVÅY UNDER ROR KANE 50-51
5080 KANALVÅY 14/14
5081 KANALVÅY 14/14
5082 ROR KANE 50-47 (LÅDNING)
5083 ROR KANE 50-47 (LÅDNING)
5084 ROR KANE 50-47 (LÅDNING)
5085 TAVNELÅTTER OVERSTISPLAN
5086 TAVNELÅTTER SVITT OG DETALJER PLÅTTELØSNING

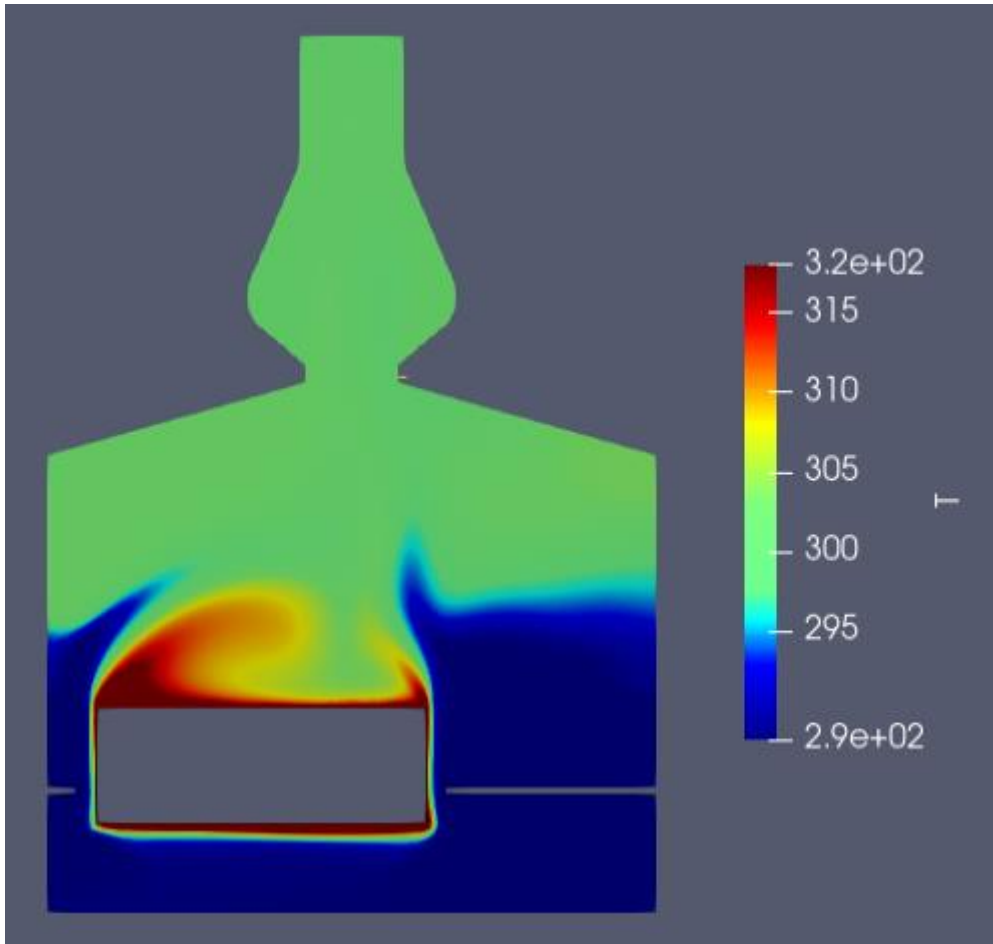
AS BUILT

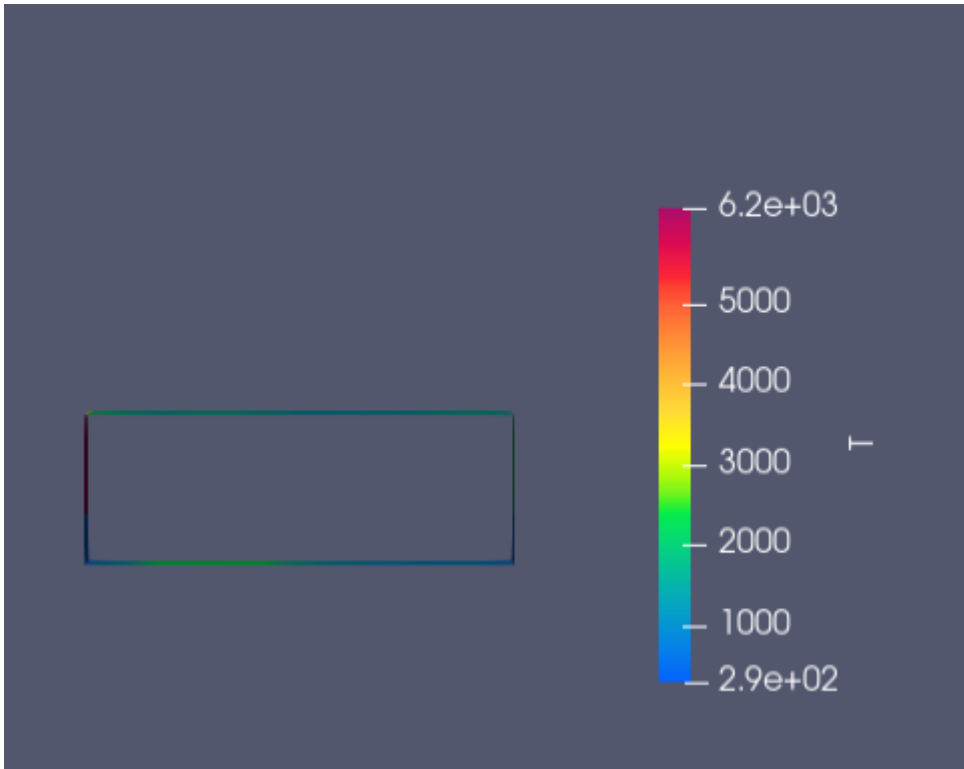
Hydro Aluminium Karmøy		Rangert/Las	
K 7	ELEKTRISK YSEANLEGG	BYGG 102	ELEKTRISK TRESHALLER
TARVENTILATORER	SVITT OG DETALJER	STÅLKONSOLISJONER	
Borealis Systemer 2783300/102 - 5251		Karmøy 2444-59	
8102-04-00	2444-59		

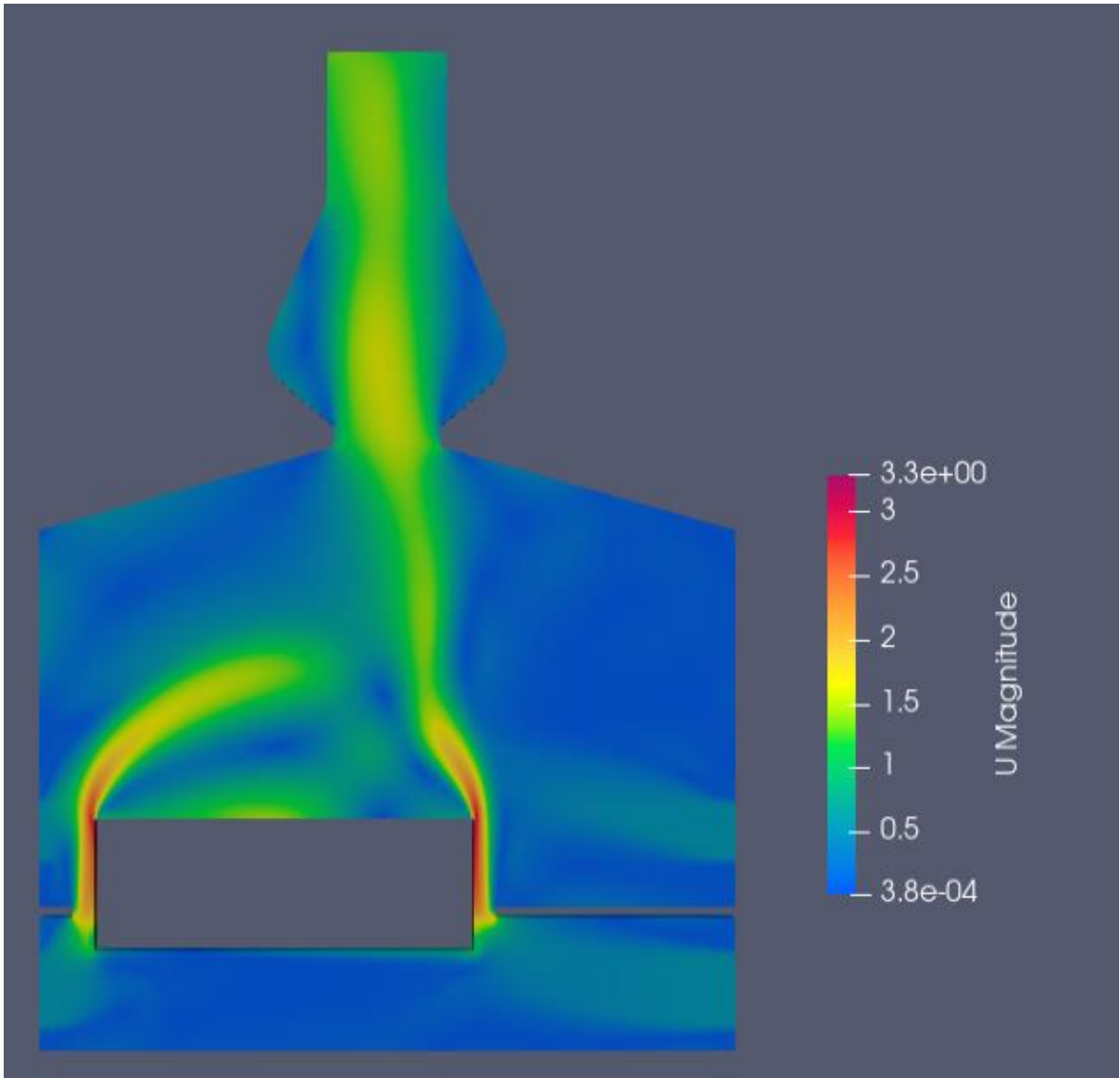


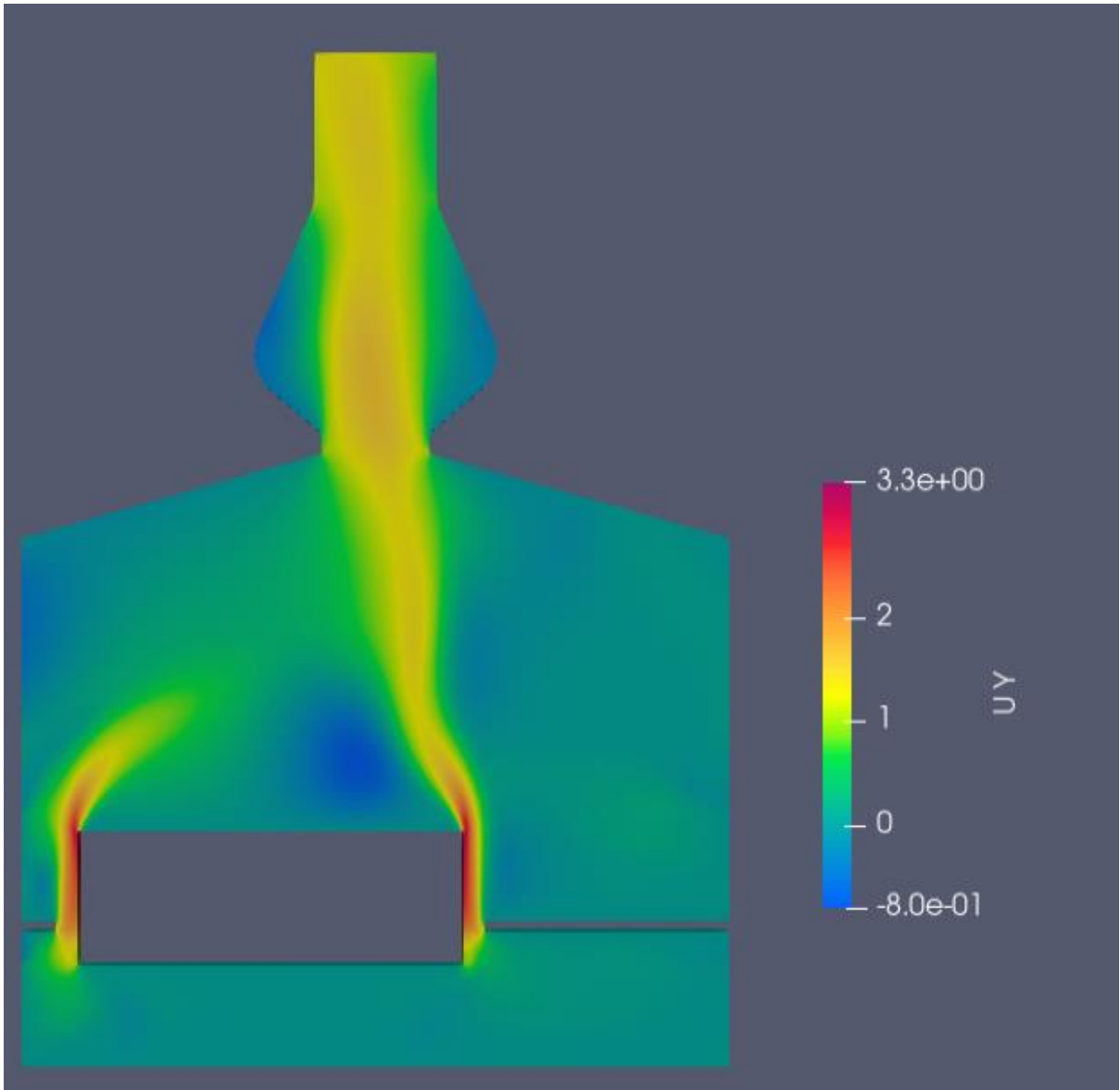
Appendix E 2D OpenFoam

Sampled data and pictures for 2D small scale pot room:

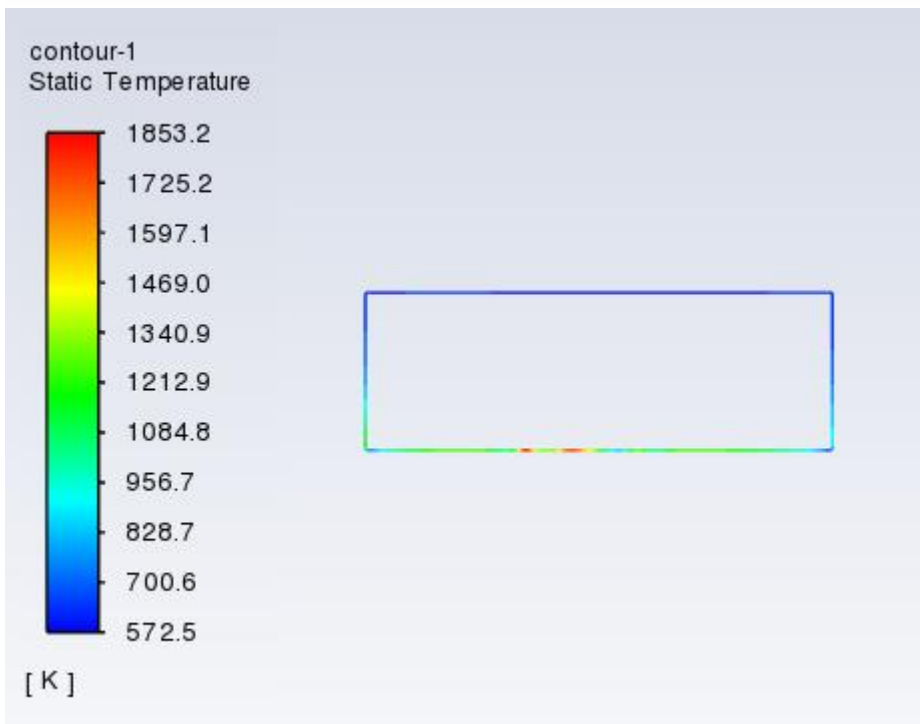
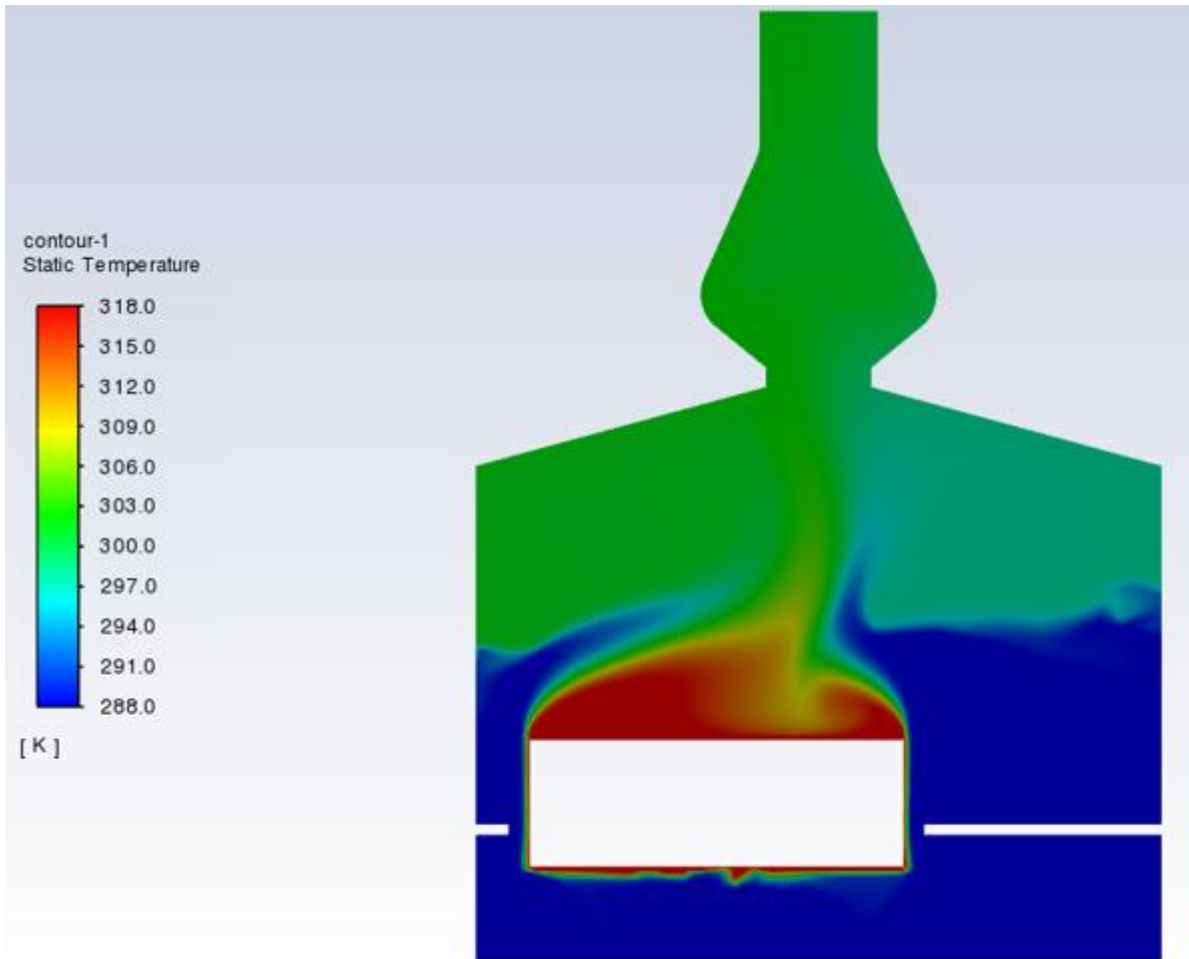








Appendix F 2D ANSYS FLUENT



Appendix G – 3D OpenFOAM

Overview of pictures of mesh and post-process, and sampled data for 3D case.

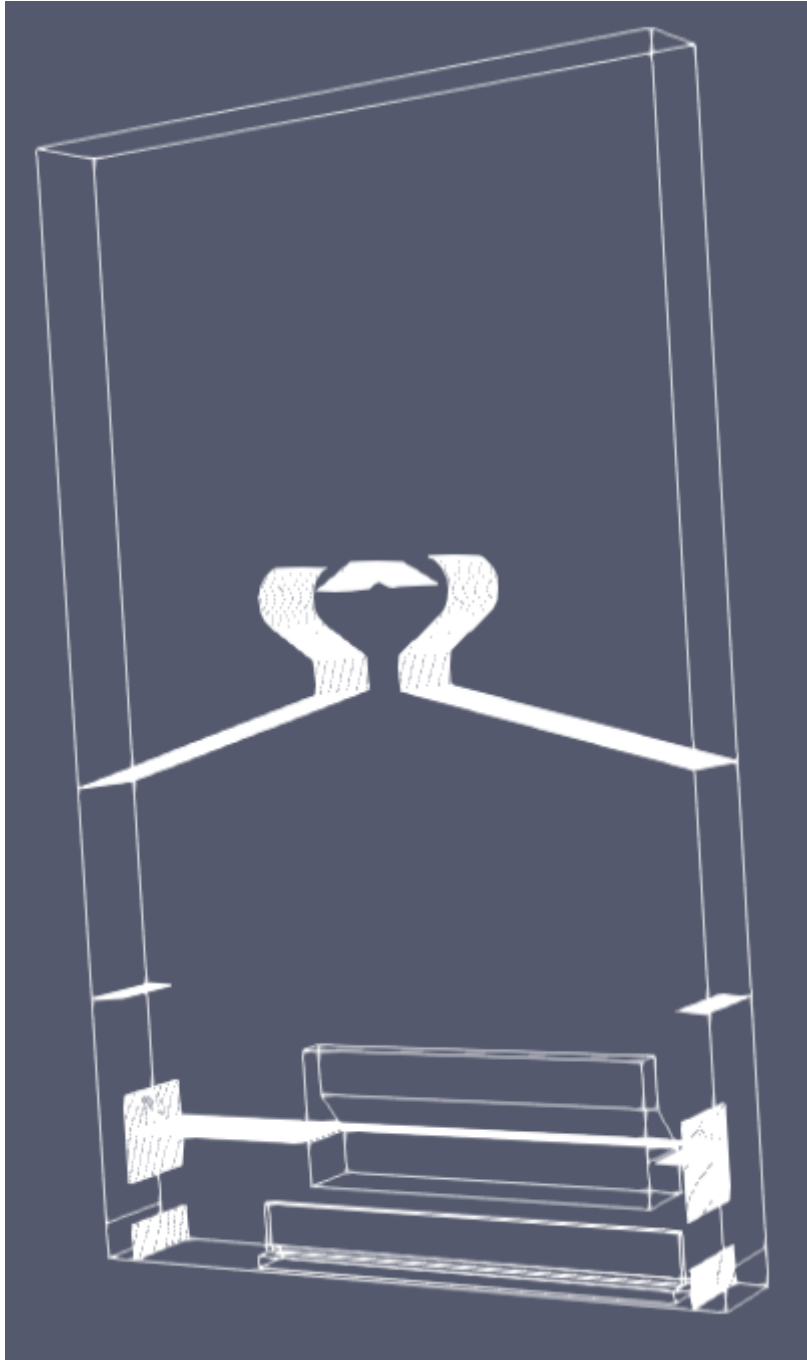


Figure 0-1: 3D mesh



Figure 0-2: Openings between pot and floor

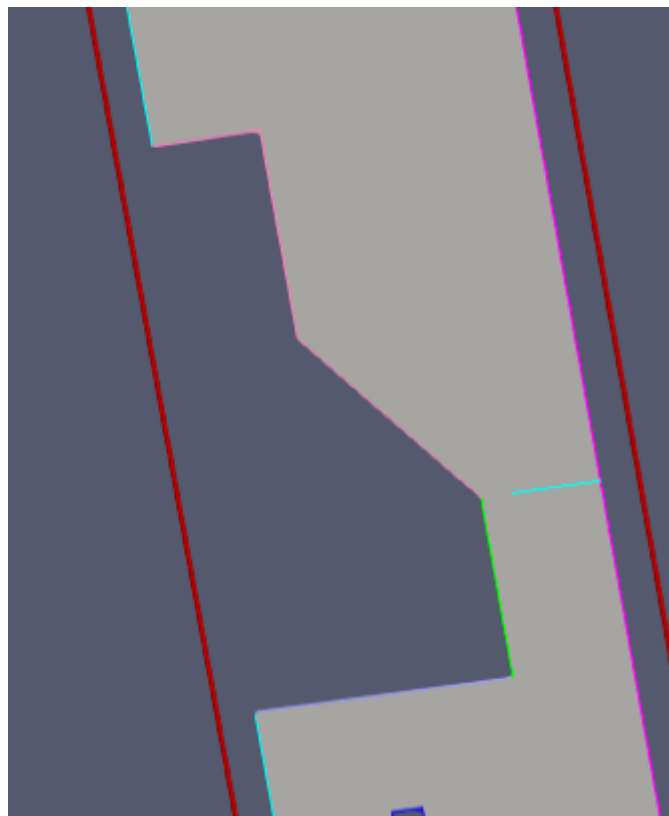


Figure 0-3: Opening between pot and floor

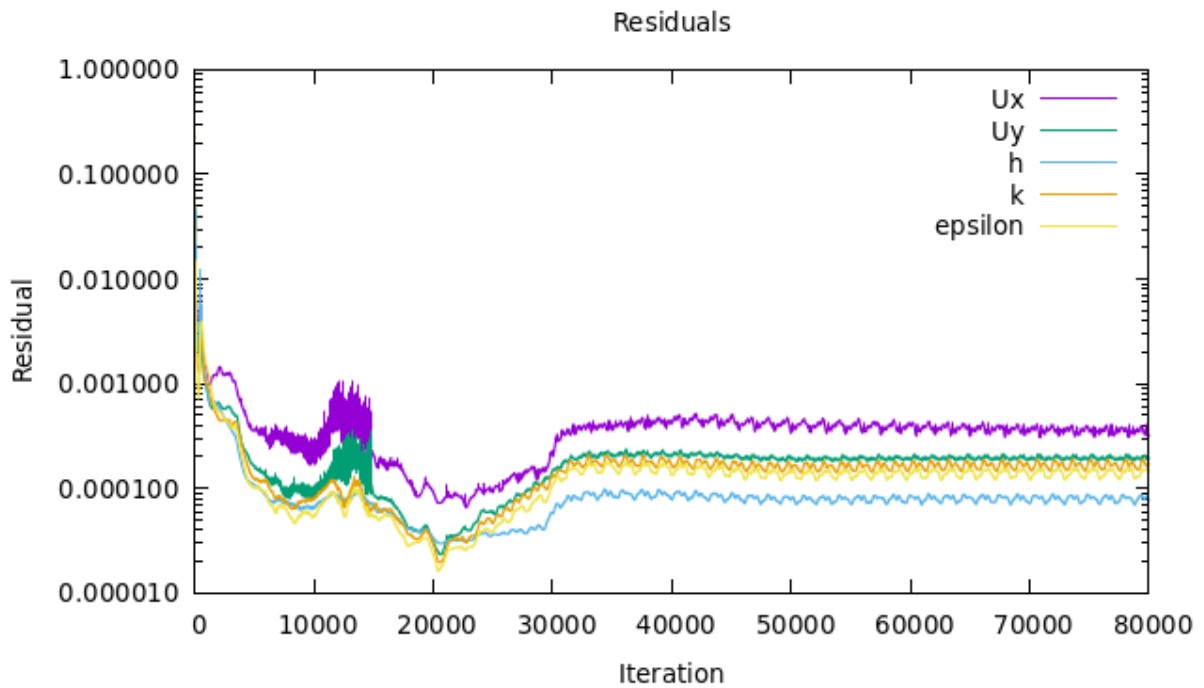


Figure 0-4: Residuals 3D

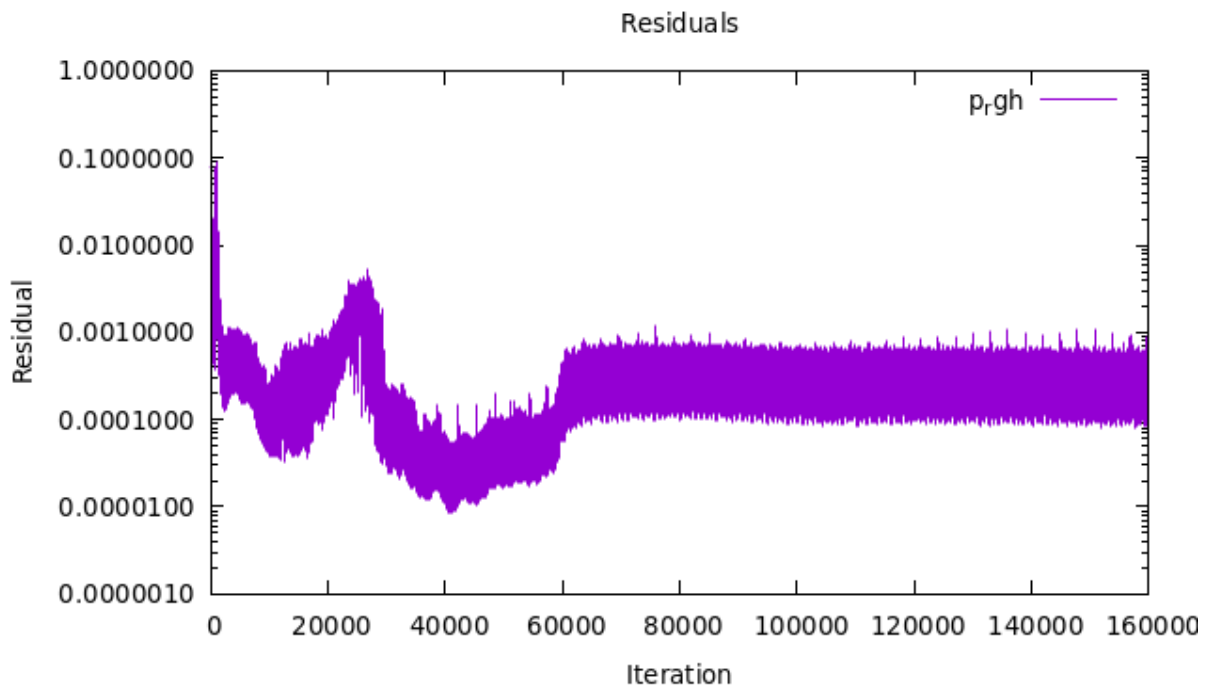
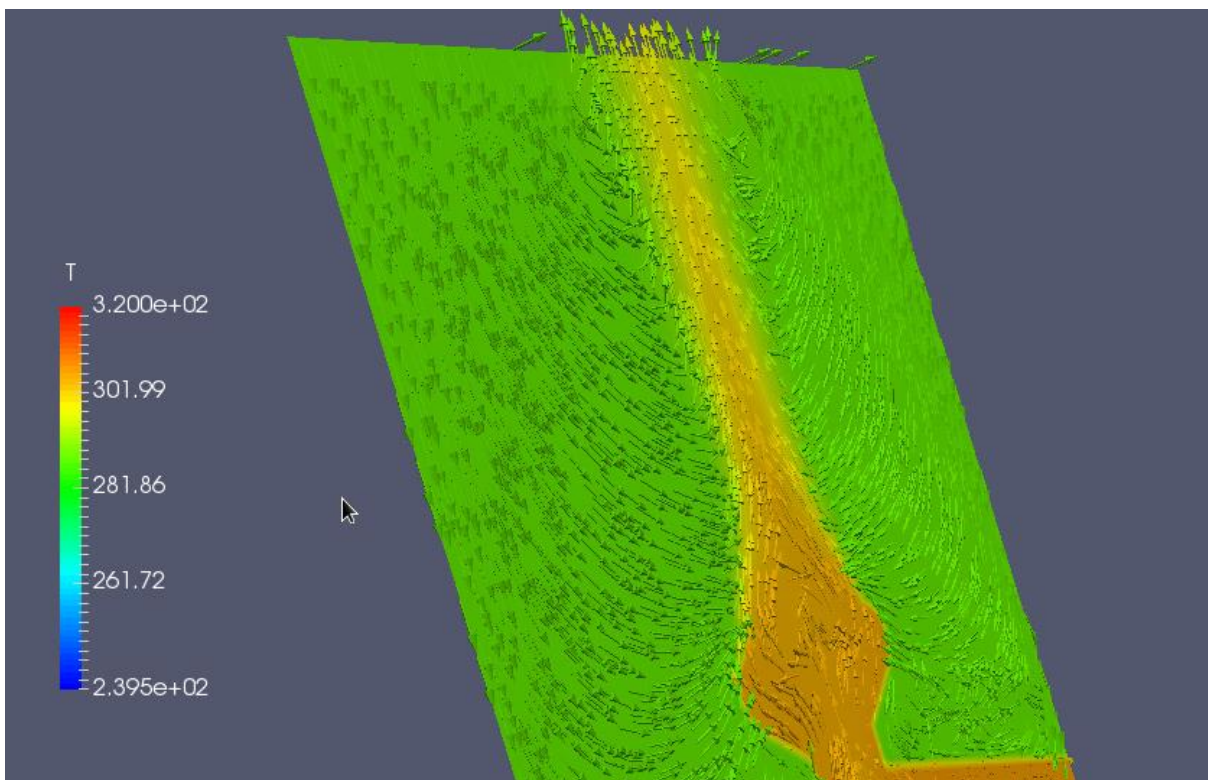
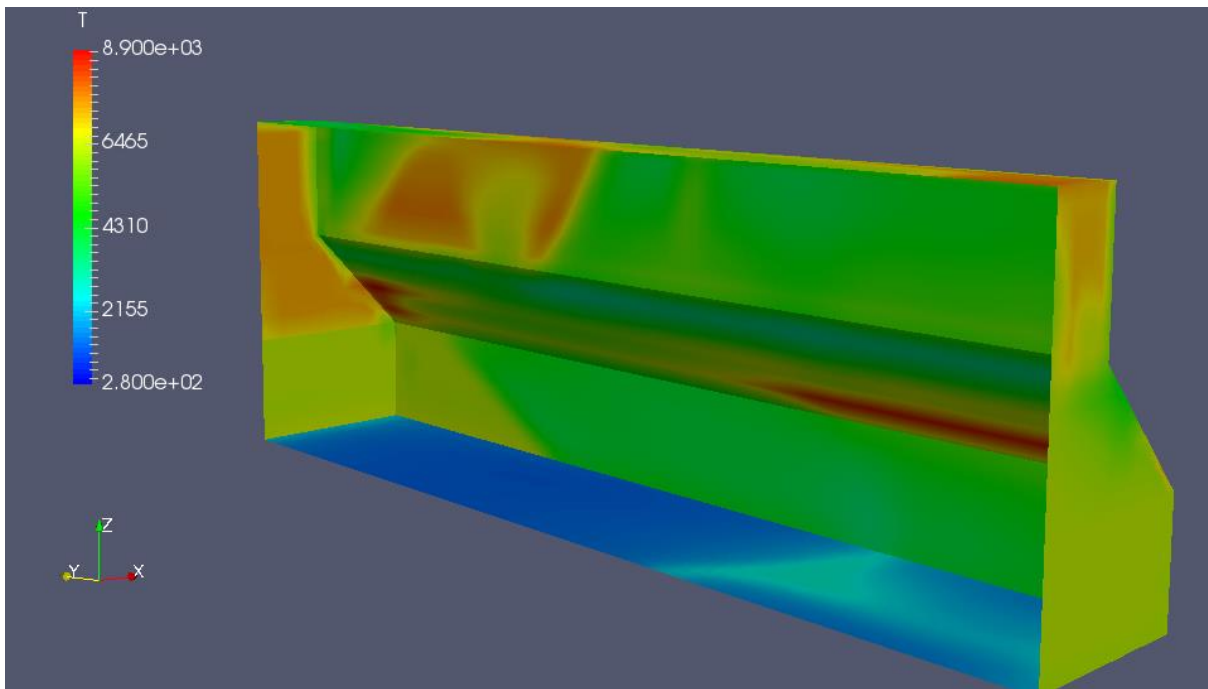
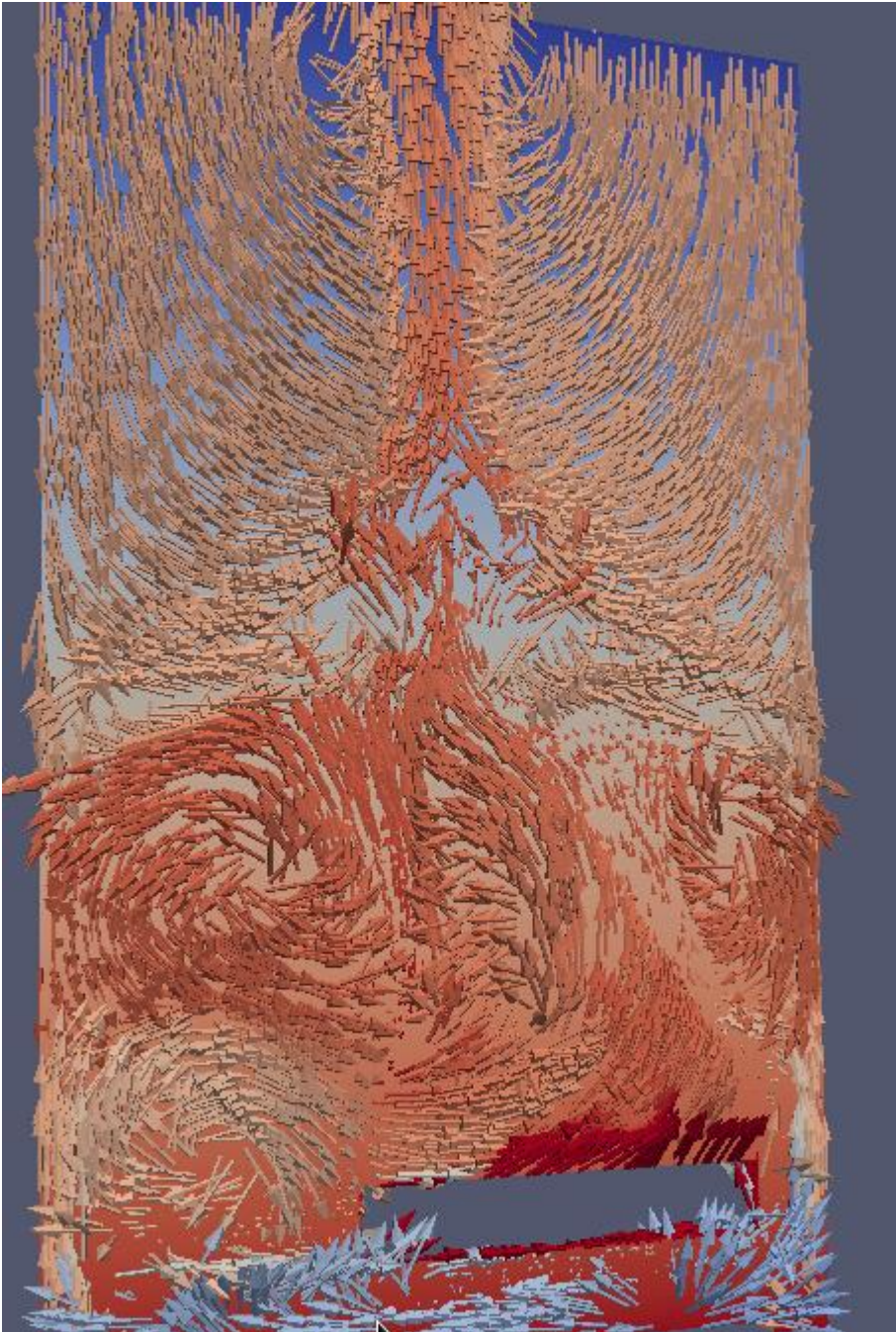


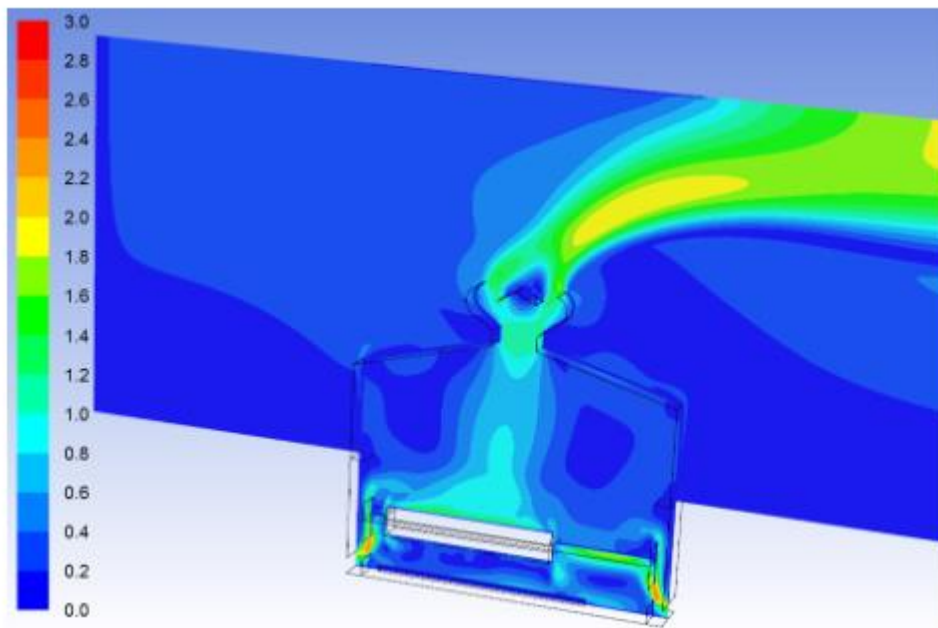
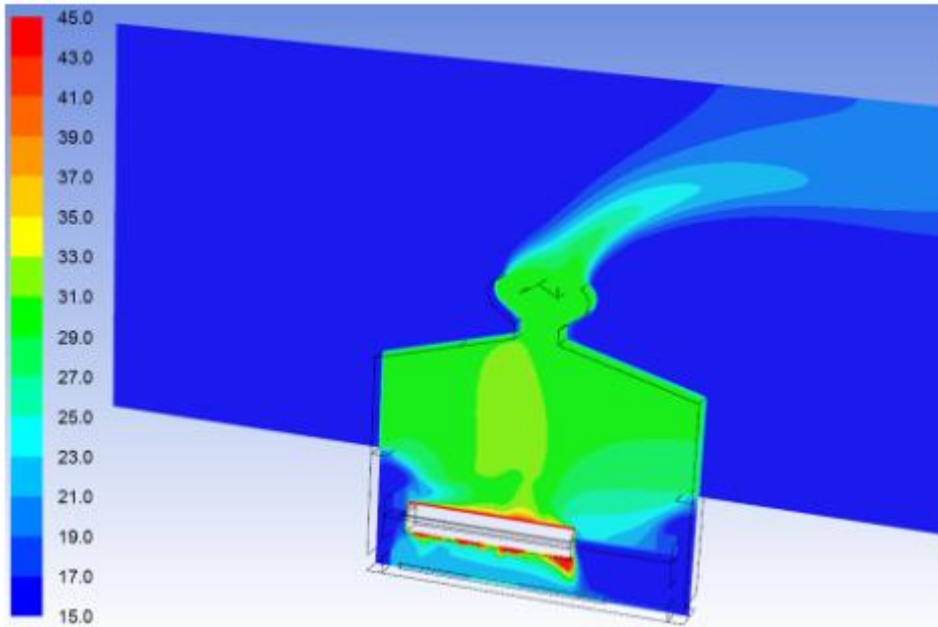
Figure 0-5: Residuals 3D for p_rgh

Sampled data in paraView, using Slice at $z=18\text{m}$, marking all cells using the tool "Select Cells Through (f)" and plotting the the data using "Plot Selection Over Time". The sampled data can be saved using the "Save data" on the top left tool bar. The correct sampled data sets are: $\text{avg}(T)$ and $\text{avg}(U(2))(z\text{-direction})$.





Appendix H- 3D ANSYS FLUENT



Appendix I y^+ measurements for 3D model

Running th

Time = 120

Reading thermophysical properties

Selecting thermodynamics package

```
{
  type      heRhoThermo;
  mixture   pureMixture;
  transport const;
  thermo    hConst;
  equationOfState perfectGas;
  specie    specie;
  energy    sensibleEnthalpy;
}
```

Reading field U

Reading/calculating face flux field phi

Creating turbulence model

Selecting turbulence model type RAS

Selecting RAS turbulence model kEpsilon

RAS

```
{
  RASModel    kEpsilon;
  turbulence   on;
  printCoeffs on;
  Cmu         0.09;
  C1          1.44;
  C2          1.92;
```

```

C3      0;
sigmaK  1;
sigmaEps 1.3;
}

```

Reading g

Reading hRef

Calculating field g.h

Reading field p_rgh

Creating field dpdt

Creating field kinetic energy K

No MRF models present

Radiation model not active: radiationProperties not found

Selecting radiationModel none

yPlus yPlus write:

writing field yPlus

patch wall-fluid-outside y+ : min = 1.43433, max = 49.496, average = 24.4399

patch wall-pot-shell-side y+ : min = 30.467, max = 86.853, average = 54.2474

patch wall-support y+ : min = 5.09687, max = 67.0211, average = 36.0186

patch wall-pot-shell-bottom y+ : min = 29.8631, max = 81.447, average = 67.793

patch wall-pot-shell-ends y+ : min = 21.6211, max = 74.4838, average = 45.13

patch wall-pot-superstructure y+ : min = 23.6328, max = 110.047, average = 75.7927

patch wall-pot-room y+ : min = 4.38315, max = 110.241, average = 43.6859

patch wall-fluid-ground y+ : min = 7.24542, max = 105.558, average = 50.2376

patch wall-internal-basement y+ : min = 16.5928, max = 100.224, average = 67.9658

patch wall-internal-monitor-internals y+ : min = 9.58231, max = 81.5342, average = 47.1445

Appendix B

patch wall-internal y+ : min = 9.87645, max = 95.4555, average = 46.976

patch wall-internal-monitor y+ : min = 3.32869, max = 97.7615, average = 27.5671

patch wall-internal-floor y+ : min = 12.5642, max = 90.5194, average = 61.1291

patch wall-internal-pot-room-roof y+ : min = 1.47812, max = 104.574, average = 33.4039

End